UNIVERSITY *of the*
WESTERN CAPE

Effect of synthetic methods on the characteristics and performance of IrO_2 catalysts

by

Simoné Karels

Thesis presented in fulfilment of the requirements for the degree of

Masters in chemistry

Department of Chemistry,

University of the Western Cape

Supervisor: Prof Sivakumar Pasupathi

Co-Supervisor: Dr Cecil Felix

December 2022

Declaration

I declare that "Effect of synthetic methods on the characteristics and performance of IrO_2 catalysts" is my work and that it has not been submitted for any degree or examination in any other university and that all the sources that I have used or quoted have been indicated and acknowledged by complete references.

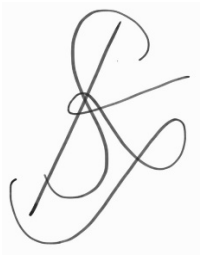

……

Simoné Karels December 2022

Acknowledgment

- Firstly, I would like to express my deepest gratitude to God for His unconditional love and grace.

- Words cannot express the gratitude I have for my mother, Marina, and brother, Damion, for their invaluable support and patience. Their belief in me has kept my motivation and spirit high during this process.

- A special thank you to the staff of the South African Institute of Advanced Material Chemistry (SAIAMC) for granting me the opportunity to conduct my MSc studies.

- Thank you to the Technology and Human Resources for Industry Program (THRIP) funding for the financial support.

- This endeavour would not have been possible without the generous support and guidance of Prof. Sivakumar Pasupathi.

- I could not have undertaken this journey without the guidance of Dr. Cecil Felix, who generously provided his support and knowledge throughout the duration of the research.

- Thank you to Dr. Subelia Botha at the Department of Physics at UWC for the HRTEM characterization of my samples.

- Thank you to Dr. Remy Bucher at iThemba Labs for the XRD characterization of my samples.

- Thank you to Dr. Hong Su at UCT for the XRD characterization of my samples.

- Lastly, I am also grateful to all my colleagues at SAIAMC for creating a friendly work environment.

Abstract

For many years fossil fuel has been the primary source of energy worldwide though, the environment is negatively affected because of the high carbon dioxide (CO_2) emissions associated with the use of fossil fuels. Hydrogen (H_2) is known for its ecological cleanliness and high energy efficiency. More consumers are considering H_2 as an energy carrier for different stationery and transportation applications. The most sustainable way to synthesize H_2 is by using the water electrolysis method with renewable energy sources like solar, wind, etc. Currently, the proton exchange membrane water electrolyzer (PEMWE), coupled with renewable energy sources, is the most efficient water electrolyzer technology to produce very pure H_2 with no CO_2 emissions. The oxygen evolution reaction (OER), which is the greatest source of overpotential, takes place at the anode of the PEMWE; therefore, the anode catalyst needs to be active and stable. However, there is a high cost associated with the anode catalyst.

An extensive amount of research has gone into synthesizing a cost-effective, high performance anode catalyst for the OER. The iridium oxide (IrO_2) catalyst has reasonable activity with high stability; however, its high cost needs to be addressed. By increasing the OER activity, the IrO_2 catalytic loading requirement can be reduced which will also reduce the high cost of the IrO_2 component. This study aims to improve the OER activity of the IrO_2 catalyst by modifying the physical properties of the IrO_2 catalyst using two different synthetic methods. The IrO_2 catalyst was synthesized using the modified Adams fusion method (MAFM) and the molten salt method (MSM). The OER performance of the IrO_2 catalysts synthesized with the MAFM and MSM were compared. The IrO_2 catalysts were also benchmarked against the 'state-of-the-art' commercial IrO_2 catalyst. Physical and electrochemical techniques were used to evaluate the IrO_2 catalysts. The physical characterization methods used were the X-ray diffraction analysis (XRD), High-resolution transmission electron microscopy (HRTEM), and the Brunauer-emmet-teller (BET). The electrochemical characterization methods used were Cyclic voltammetry (CV), Linear sweep voltammetry (LSV), and Chronopotentiometry (CP) to study the IrO_2 catalytic activity and stability.

List of Figures

List of tables

List of abbreviations

ATR	Auto thermal reforming
AWE	Alkaline water electrolyzer

BET	Brunauer-emmet-teller
CE	Counter electrode
CP	Chronopotentiometry
CV	Cyclic voltammetry
HER	Hydrogen evolution reaction
HRTEM	High-resolution transmission electron microscopy
LSV	Linear sweep voltammetry
MAFM	Modified Adams fusion method
MEA	Membrane electrode assembly
MSM	Molten salt method
OER	Oxygen evolution reaction
PEMWE	Proton exchange membrane water electrolyzer
PGM	Platinum group metals
POx	Partial oxidation
RE	Reference electrode
SEM	Scanning electron microscopy
SOWE	Solid oxide water electrolyzer
SR	Steam reforming
STP	Standard temperature and pressure
WE	Working electrode
YSZ	Yttrium stabilized zirconia

Table of contents

Chapter 1: Introduction

1.1 Hydrogen as an energy carrier

The growth in the global population and industrial development has caused an increase in the global energy demand. Currently, most countries are relying on fossil fuels for their energy needs [1, 2, 3]. The main disadvantages associated with fossil fuels include greenhouse gas and SO_x, CO_x, NO_x, etc. emissions. A recent study by Holladay et al. [6] predicts that pollution will have serious effects on public health if global emission continues to increase. This led many researchers to focus their attention on renewable energy sources like solar, wind, geothermal, and tidal energy. The main challenges related to these technologies are obtaining renewable energy sources which are sustainable, abundant, and the energy can be safely stored [1, 7]. Battery storage is one option, but the disadvantages associated include the loss of charge with time and the high cost of large storage, which makes it less ideal [8]. Hydrogen (H_2) is a suitable energy storage medium since it is potentially the cleanest available fuel with only water (H_2O) as the by-product [1, 3, 4, 9]. A small amount of H_2 is used as fuel to operate motor vehicles. Future H_2 applications will include the supply of power and heating to the residential sectors [7, 10].

Several issues need to be overcome for H_2 to be practical as a fuel worldwide. One of the issues is the use of high amounts of energy to produce the H_2 molecule since H_2 is usually bound to other elements in H_2O or hydrocarbons [7, 11, 12]. Cost and energy-efficient methods for the delivery, purification, and design of systems with increased H_2 energy are required. Furthermore, the upscale of the technical processes needed to be inexpensive, energy-efficient, durable, and have an improved lifetime since H_2 will play an important role in the future as a viable energy carrier [1, 13].

1.2 Hydrogen production

The study of H_2 production and its commercial usage dates to the 1800s [6, 13]. Today, about 0.1 GT of H_2 is annually produced and is primarily consumed on-site, used for metal treatment, and refining. There are different pathways, feedstock, and technologies to synthesize H_2. The technology used to synthesize H_2 determines the efficiency, purity, and cost-effectiveness [13]. The synthesized H_2 can be classified into two main

categories depending on the feedstock used i.e., conventional, and renewable energy sources as shown in Figure 1.1 [7].

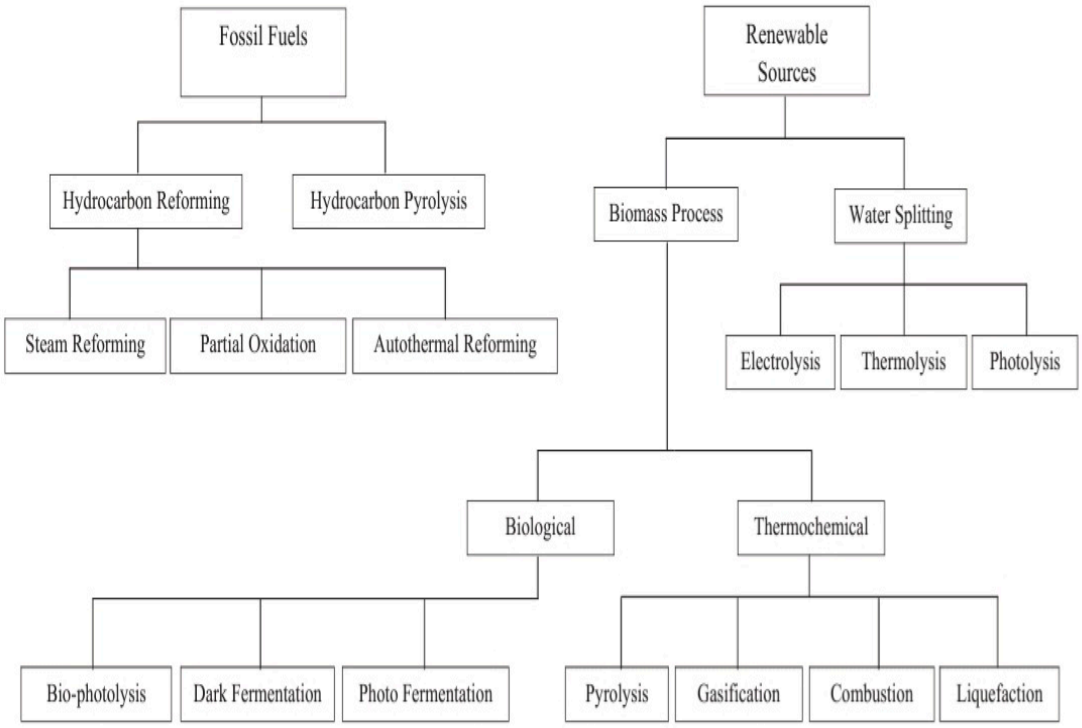

Figure 1.1: H_2 production methods.

The methods to synthesize H_2 from renewable energy sources include biomass and the water-splitting method. The biomass methods are carbon dioxide (CO_2)-neutral, clean, and abundant, however, varying amounts of H_2 are synthesized, depending on the seasonal feedstock and availability. When using water-splitting methods such as photolytic, thermal, and electrolytic processes, only H_2 and oxygen (O_2) gas are produced from H_2O [7]. Therefore, the little to no global pollution of the water-splitting method has caught the attention of many researchers.

1.2.1 Photolytic hydrogen production

H_2 production using solar energy is an ideal method to produce sustainable energy. Photolytic H_2 production can be applied in three different approaches i.e., the PV-electrolysis system, suspension-based system, and the photo-electrochemical cell [14].

All three approaches use a photo-electrode semiconductor like the one used in photovoltaics to absorb rays from the sun. The photo-electrode semiconductor provides the required voltage to decompose H_2O into H_2 and O_2 gas [6, 7, 14]. Equations 1-3 show the reactions which take place during photolytic H_2 production.

Anode: $2p^+ + H_2O \rightarrow \frac{1}{2} O_2 + 2H^+$ (1)

Cathode: $2e^- + 2H^+ \rightarrow H_2$ (2)

Overall: $H_2O \rightarrow H_2 + \frac{1}{2} O_2$ (3)

Different materials in photo-electrodes have been studied including thin-film TiO_2, WO_3, Fe_2O_3 n-GaN, n-GaAs, and ZnS. CdS are used for the photo-anode and p-SiC/PtClGS/Pt, and p-InP/Pt for the photo-cathode [6, 7, 14, 15]. The semiconductor substrate and photo-electrode materials determine the system's performance. The photo-electrode materials can create holes that cause surface oxidation. This results in either the semiconductor surface layer being blocked, or the electrode being corroded [6].

The overall efficiency (<5%) of the photolytic H_2 production is lower when compared to the thermal and electrolytic H_2 processes. Researchers need to develop innovative materials, design new concepts, and develop novel synthetic methods which are safe for solar H_2 energy to be effective [16].

1.2.2 Thermal process of hydrogen production

About 96% of the global H_2 is synthesized with thermal processes, also known as reforming, of fossil fuels. During the thermal processes, a gas stream consisting of H_2, CO, and CO_2 is produced. The three main thermal processes are auto-thermal reforming (ATR), steam reforming (SR), and partial oxidation (POX) [17, 18].

SR is mainly used due to its high efficiency, lower operating temperatures, lower cost, and higher H_2/CO ratio when compared to ATR and POx. Only two steps take place during the SR process. In the first step, steam is reacted with hydrocarbons to synthesize syn-gas (H_2 and CO). In the second step, the CO is reacted with steam to synthesize H_2

and CO_2. The reaction is performed in the presence of a copper catalyst to increase the total H_2 production [17, 18].

PO_X is a non-catalytic process that converts hydrocarbons into H_2 by partially oxidizing O_2 gas. No external heat sources are required as POx synthesizes heat [18]. With the addition of steam, POx is like ATR. Oil (18%), coal (30%), and natural gas (48%) can also be used to synthesize H_2 from POx. However, these energy sources produce large amounts of Co, making them non-sustainable [4, 19].

Pyrolysis is another thermal process that disintegrates hydrocarbon into carbon and H_2 [17]. A large emission reduction is caused when using any organic material during the process. No air and H_2O are present, eliminating the need for a second reactor which prevents the formation of CO [6].

1.2.3 Electrolytic hydrogen production

When using electricity to synthesize H_2 from H_2O the process is called water electrolysis. Water electrolysis was discovered in the 1800s and became popular during the 1920s and 1930s [9]. Today, only 4% of the overall H_2 production uses water electrolysis [14, 16, 20]. H_2O will be the next coal since it is more sustainable when compared to other renewable energy sources i.e., solar energy, wind energy, biomass, etc. The advantages associated include the production of pure H_2, simple small-scale/real-time H_2 supply, utilization of renewable primary energy sources, no dependence on hydrocarbon sources, and no carbon emissions. The efficiency of commercial electrolyzers ranges between 56-73% [6, 21]. At atmospheric temperature and pressures, about 8.9 L of H_2O and 39 kWh of energy are used to synthesize 1 kg of H_2. Water electrolysis is used in applications like food, electronics, marine, space crafts, and rocket industries where large-scale pure H_2 is required [9, 22]. The main disadvantage of water electrolyzers is the related high cost (>$20/GJ) [12]. Recently, high pressure (pressures > 1000 psig) electrolyzers are being developed to eliminate the associated high cost H_2 compressors [6, 21].

1.3 Theory of water electrolysis

H_2O is a very stable compound, and an energy supply is essential to split H_2O into H_2 and O_2 gas. The total energy to split an H_2O molecule is known as the H_2O formation enthalpy. The enthalpy changes, $\Delta H° = 286$ $kJmol^{-1}$, at increased H_2 heating values

under standard temperature, 298.15 K, and pressure,1 atm (STP). Subsequently, changing both the free energy, $\Delta G° = 237.2$ kJmol^{-1}, and the entropy, $\Delta S° = 0.163$ kJmol^{-1}K^{-1} [23, 16, 20, 24]. A lower heating value, 242 kJmol^{-1}, is required when steam is used [25].

All chemical reactions use some of the energy for the entropy change. Both the free energy change and the reaction enthalpy are related to the entropy change, as shown in Equations 4 and 5 [16, 23].

$$\Delta G = \Delta H - T\Delta S \quad (4)$$

The entropy change is determined by calculating the difference between the enthalpy change and the free energy change.

$$T\Delta S° = \Delta H° - \Delta G° = 285.83 - 238 = 47 \text{ kJmol}^{-1} \quad (5)$$

During the water-splitting process, at STP, 47 kJmol^{-1} of energy is spontaneously absorbed from the environment and used for the entropy change. About $\Delta G° = 237.2$ kJmol^{-1} electrical energy is also required (Equation 6) [16, 26].

$$H_2O + \text{heat } (T\Delta S) + \text{electrical energy } (\Delta G) \rightarrow H_2 + \frac{1}{2}O_2 \quad (6)$$

The amount of electricity required can be calculated when using Equation 7 [23].

$$E° = \frac{\Delta G°}{nF} \quad (7)$$

The equilibrium cell potential (E°), also known as the minimum potential, is calculated by subtracting the equilibrium potentials of the cathode from the anode (Equation 8). The Faraday constant (F) is equal to 96485 $Cmol^{-1}$ and the number of electrons transferred per H_2 mole is n = 2. When substituting the values into Equation 7 the obtained potential is equal to +1.23 V vs. reversible hydrogen electrode (RHE), as shown in Equation 9 [14, 16, 20, 23, 27].

$$E° = E^{\circ}_{anode} - E^{\circ}_{cathode} \quad (8)$$

$$E° = \frac{237.2 \text{kJmol}-1}{2\ x\ 96485\ Cmol-1} = +1.23 \text{ V vs. RHE} \quad (9)$$

A thermo-neutral potential (E°_{th}) of +1.48 V vs. RHE is applied in an isolated system to satisfy the thermodynamic conditions (Equation 10).

$$E^{\circ}_{th} = \frac{\Delta H}{nF} = \frac{285.8 \text{ kJmol}-1}{2\ x\ 96485\ Cmol-1} = +1.48 \text{ V vs. RHE} \quad (10)$$

The chemical reactions will be exothermic and endothermic above and below +1.48 V vs. RHE, respectively. Most electrolyzers operate at potentials greater than +1.27 V vs. RHE, resulting in cell heating [11, 20, 23, 27, 29].

1.4 Types of water electrolyzers

The main types of electrolyzers are (i) alkaline water electrolyzer (AWE), (ii) solid oxide water electrolyzer (SOWE), and (iii) proton exchange membrane water electrolyzer (PEMWE), depending on the electrolyte used.

1.4.1 Alkaline water electrolyzer

The AWE is the first electrolyzer to be studied in 1789 by Troostwijk and Diemann [30]. AWE is a well-developed technology that synthesizes H_2 on a commercial scale. It is composed of two electrodes (anode and cathode) which are separated by a diaphragm,

an aqueous alkaline electrolyte, and a microporous separator, as shown in Figure 1.2 [20, 27, 31-36].

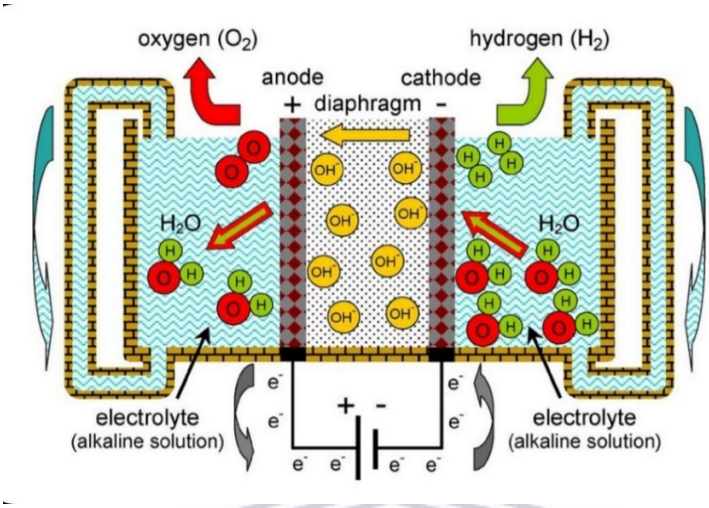

Figure 1.2: Scheme of the operating principle of an AWE.

During the AWE process, H_2O is introduced at the cathode where it separates into H_2 and OH^-, as shown in Equation 11. The H_2 remains in the alkaline solution, whereas the OH^- ion travels across the diaphragm to the anode within the electrical field. The electrical field is provided by an external power source. The OH^- ion recombines on the anode surface to form O_2 gas (Equation 12). A gas-liquid separation unit outside the system separates the H_2 from the H_2O. Equation 13 summarizes the overall fundamental AWE reaction [6, 20, 32].

Cathode: $2H_2O + 2e^- \rightarrow H_2 + 2OH^-$ (11)

Anode: $4OH^- \rightarrow O_2 + 2H_2O$ (12)

Overall: $H_2O \rightarrow H_2 + \frac{1}{2}O_2 \qquad \Delta H = -286\ kJmol^{-1}$ (13)

The AWE is made up of steel materials [31]. The most common materials used for the anode are copper and nickel, which are coated with a metal oxide. For the cathode, nickel is generally used with a platinum coating [20, 28, 35]. About 10-40 wt% NaOH or KOH electrolytes are used due to their high conductive composition [24]. The AWE operates at increased temperatures (>120℃) and at a current density of < 400 $mAcm^{-2}$. The increased temperatures allow the solidification of the electrolytes. This increases the electrolyte conductivity and concentration while improving the electrode surface reaction kinetics [27, 20, 37]. The obtained efficiency ranges between 40-80% [6, 9, 27, 20, 29, 31, 35]. The AWE are the system's lower cost and large-scale development [38].

The oxidized half-reaction at the anode is the most demanding aspect of the AWE and its catalytic material still required significant development [27]. Another disadvantage related to the AWE is the possibility of atmospheric CO_2 reacting with the KOH electrolyte to synthesize carbonates. Some systems still use the liquid alkaline solution as the electrolyte, resulting in low current densities, and high maintenance costs [15, 38].

1.4.2 Solid oxide water electrolyzer

The SOWE synthesizes H_2 from H_2O by replacing part of the required electrical energy with thermal energy. During the SOWE reaction, steam is passed through the cathode to form H_2 and O^{2-} ions (Equation 14). The O^{2-} ion goes through the electrolyte to the anode where O_2 gas is synthesized while releasing electrons (Equation 15). The overall chemical reaction of SOWE is summarized in Equation 16 [4, 27, 34, 39, 40]

Cathode: $H_2O + 2e^- \rightarrow H_2 + O^{2-}$ (14)

Anode: $O^{2-} \rightarrow \frac{1}{2} O_2 + 2e^-$ (15)

Overall: $H_2O \rightarrow H_2 + \frac{1}{2} O_2 \qquad \Delta H = -286\ kJmol^{-1}$ (16)

The SOWE is composed of two electrodes (anode and cathode) and a solid electrolyte, as shown in Figure 1.3 [27]. A typical solid oxide electrolyte is made up of a thin gas-tight film of Yttrium-Stabilized Zirconia (YSZ) [6, 11, 27, 31, 33, 40, 41]. Both noble

and non-noble metals are used for the cathode. Noble metals include gold, platinum, and the platinum group metal (PGM) while non-noble metals are the rest of the transition group metals. For the anode, YSZ and perovskites like ferrites, $LaFeO_3$, or lanthanum manganites, $LaMnO_3$, are used. In very oxidized environments, only noble metals and electronically conductive mixed oxide materials are used as anodes. However, the highest ionic conductivity is shown when Sc_2O_3 is doped with ZrO_2. The reason for the high ionic conductivity is due to the ionic radius of Zr^{4+} being closest to the ionic radius of Sc^{3+} [40].

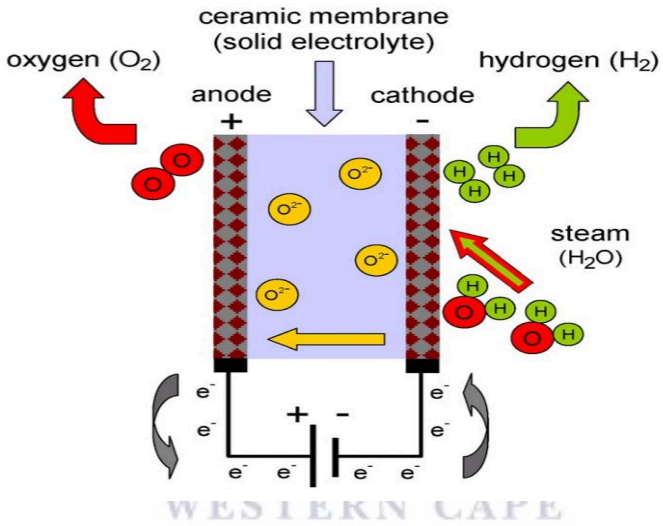

Figure 1.3: Scheme of the operating principle of a SOWE.

During the SOWE process, low electrical energy is required at high operating temperatures (600-900℃) [27]. High efficiencies are obtained at these high operating temperatures [6, 11, 27, 40]. However, when including thermal sources, the efficiency drops significantly [6]. A solid electrolyte eliminates the liquid and flows distribution concerns. Some renewable energy sources like geothermal energy can act as a heat source in the SOWE [27].

The main disadvantages related to the SOWE are long-term electrode deactivation and electrolyte aging [20, 27, 34, 39]. The SOWE has low cell voltage, high heat demand, and sealing issues [6, 27, 31]. Surface fusion, adsorption/desorption, and reaction kinetics are other concerns related to the SOWE [34]. The additional facilities required

to separate H_2 from steam and the noble metal electrodes add to the associated high cost of the SOWE [6, 27]. For the large-scale commercialization of SOWE, researchers need to focus on the abovementioned issues.

1.4.3 Proton exchange membrane water electrolyzer

The PEMWE, also known as the solid polymer electrolyte, was first developed in 1966 by General Electric Co. The development of PEMWE was part of a space program during the introduction of a per-fluorinated cation exchange membrane [9, 20, 27, 34]. During the PEMWE process, deionized H_2O is supplied at the anode where the H_2O molecules are split into electrons, protons, and O_2 gas, as shown in Figure 1.4 [6, 9, 27, 36, 42-44]. The electrons move through the external circuit while the protons move to the cathode, through the proton exchange membrane. The electrons combine with the protons at the cathode to synthesize H_2. Furthermore, the O_2 gas is synthesized at the anode [6, 27, 44].

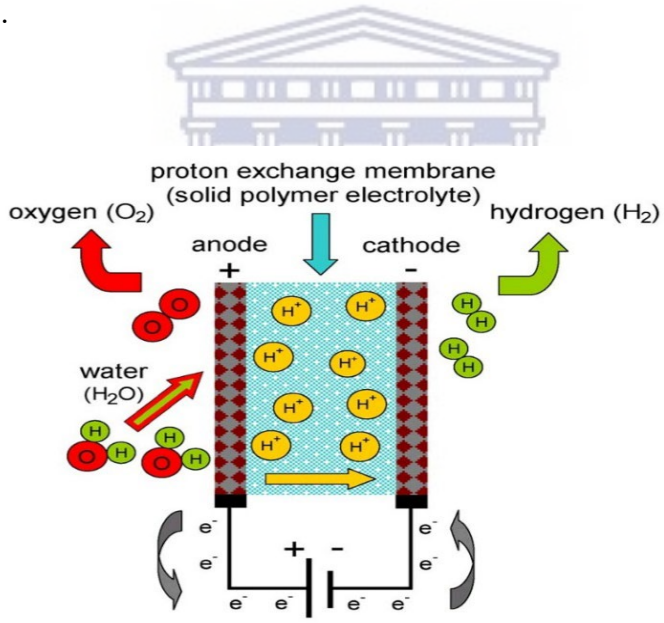

Figure 1.4: Scheme of the operating principle of a PEMWE.

The PEMWE reaction involves the splitting of 2 moles of H_2O to synthesize 2 moles of H_2 and 1 mole of O_2, as shown in Equations 17-19 [7, 16, 27, 44, 45].

Anode: $2H_2O \rightarrow O_2 + 4H^+ + 4e^-$ (17)

Cathode: $4H^+ + 4e^- \rightarrow 2H_2$ (18)

Overall: $H_2O \rightarrow H_2 + \frac{1}{2}O_2 \qquad \Delta H = -286\ kJmol^{-1}$ (19)

The active sites where the ions, gas species, and electrons meet are called the Triple Phase Boundary [42]. A diaphragm, also called a separator, needs to be implemented to separate the combination of O_2 and H_2 at the electrodes. The diaphragm also prevents the short-circuiting of the electrodes [9, 42, 43]. When the anode and cathode are bonded to the membrane, the assembled stack is called the membrane-electrode assembly (MEA) [20, 42, 46, 47,]. The porous anodic and cathodic catalytic layers are in direct contact with the membrane [28]. The solid electrolyte should not react with the electrodes. While, the electrodes need to have good electrical conductivity, be resistant to corrosion, and show the correct structural reliability [27, 36]. The MEA is compressed between two porous current distributors which are usually synthesized with sintered titanium particles [36, 42]. Two bipolar plates are used to send electric current to the cells whilst separating them [44]. The contact points between the catalyst and current collector are critical as they allow a good distribution of the current at the interfaces. End plates are connected to a direct current external power supply [41, 42].

At low temperatures, PEMWE is the most efficient and attractive method to produce H_2 from H_2O. PEMWE can operate at current densities >1500 $mAcm^{-2}$ and maintain efficiencies between 55-80% due to the low ionic resistance [6, 9, 20, 27-29, 34, 36, 42-44]. A high level of safety, ecological cleanliness, high gas purity, higher production rate, smaller mass-to-volume ratio, and low power cost is associated with PEMWE [6, 9, 35]. Conventional PEMWE has a very short life but after introducing Nafion® by DuPont, the life span of the PEMWE has increased significantly. Nafion®, a soft matter material, is a popular membrane made up of per-fluorinated acid with a sulfonic acid end group [27, 28, 42, 46]. The thickness of Nafion® is ∼10-15 × thicker than the membranes used in fuel cells [47].

Even though the PEMWE is commercially available, some associated drawbacks require special attention. Only noble metal catalysts are suitable for the PEMWE due to the acidic nature of Nafion® [6, 31, 35, 42, 46]. Recently, the focus of the PEMWE is

the improvement of (i) low-cost, stable, and active oxygen evolution reaction (OER) catalysts, (ii) low-cost membranes alternative to Nafion®, and (iii) high temperature PEMWE [27, 42, 31, 29, 35, 48]. Table 1.1 summarizes the characteristics, advantages, and challenges related to the main electrolyzers available [31].

Table 1.1: Characteristics of the main electrolyzers available.

	Low Temperature Electrolysis			High Temperature Electrolysis		
	Alkaline (OH^-) electrolysis		Proton Exchange (H^+) electrolysis	Oxygen ion(O^{2-}) electrolysis		
	Liquid	Polymer Electrolyte Membrane		Solid Oxide Electrolysis (SOE)		
	Conventional	Solid alkaline	H^+ - PEM	H^+ - SOE	O^{2-} - SOE	Co-electrolysis
Operation principles	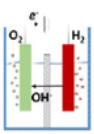	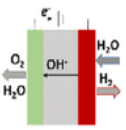	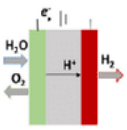	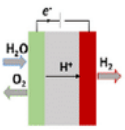	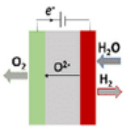	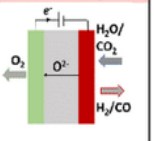
Charge carrier	OH^-	OH^-	H^+	H^+	O^{2-}	O^{2-}
Temperature	20-80°C	20-200°C	20-200°C	500-1000°C	500-1000°C	750-900°C
Electrolyte	liquid	solid (polymeric)	solid (polymeric)	solid (ceramic)	solid (ceramic)	solid (ceramic)
Anodic Reaction (OER)	$4OH^- \rightarrow 2H_2O + O_2 + 4e^-$	$4OH^- \rightarrow 2H_2O + O_2 + 4e^-$	$2H_2O \rightarrow 4H^+ + O_2 + 4e^-$	$2H_2O \rightarrow 4H^+ + 4e^- + O_2$	$O^{2-} \rightarrow {}^1/_2O_2 + 2e^-$	$O^{2-} \rightarrow {}^1/_2O_2 + 2e^-$
Anodes	Ni > Co > Fe (oxides) Perovskites: $Ba_{0.5}Sr_{0.5}Co_{0.8}Fe_{0.2}O_{3-\delta}$, $LaCoO_3$	Ni-based	IrO_2, RuO_2, $Ir_xRu_{1-x}O_2$ Supports: TiO_2, ITO, TiC	Perovskites with protonic-electronic conductivity	$La_xSr_{1-x}MnO_3$ + Y-Stabilized ZrO_2 (LSM-YSZ)	$La_xSr_{1-x}MnO_3$ + Y-Stabilized ZrO_2 (LSM-YSZ)
Cathodic Reaction (HER)	$2H_2O + 4e^- \rightarrow 4OH^- + 2H_2$	$2H_2O + 4e^- \rightarrow 4OH^- + 2H_2$	$4H^+ + 4e^- \rightarrow 2H_2$	$4H^+ + 4e^- \rightarrow 2H_2$	$H_2O + 2e^- \rightarrow H_2 + O^{2-}$	$H_2O + 2e^- \rightarrow H_2 + O^{2-}$ $CO_2 + 2e^- \rightarrow CO + O^{2-}$
Cathodes	Ni alloys	Ni, Ni-Fe, $NiFe_2O_4$	Pt/C MoS_2	Ni-cermets	Ni-YSZ Subst. $LaCrO_3$	Ni-YSZ perovskites
Efficiency	59-70%		65-82%	up to 100%	up to 100%	-
Applicability	commercial	laboratory scale	near-term commercialization	laboratory scale	demonstration	laboratory scale
Advantages	low capital cost, relatively stable, mature technology	combination of alkaline and H^+-PEM electrolysis	compact design, fast response/start-up, high-purity H_2	enhanced kinetics, thermodynamics: lower energy demands, low capital cost		+ direct production of syngas
Disadvantages	corrosive electrolyte, gas permeation, slow dynamics	low OH^- conductivity in polymeric membranes	high cost polymeric membranes; acidic: noble metals	mechanically unstable electrodes (cracking), safety issues: improper sealing		
Challenges	Improve durability/reliability; and Oxygen Evolution	Improve electrolyte	Reduce noble-metal utilization	microstructural changes in the electrodes: delamination, blocking of TPBs, passivation		C deposition, microstructural change electrodes

1.5 Catalyst for PEMWE

The catalyst plays an important role in H_2O electrolyzer performance by increasing the H_2 production and reducing the energy requirement [13]. Micrometre thick catalytic layers may include supported or unsupported particles that are filled with ionomer chains [42]. The catalytic layer structure must be highly porous and conductive to let gases move away from the interface to allow a homogenous current flow [13, 20, 46]. Many researchers are studying the content reduction of PGM by either using metal oxides at the anode or metal alloys at the cathode [20, 42, 47]. The PGM includes Ru,

Rh, Pd, Os, Ir, and Pt [30]. For the PEMWE, IrO_2 and RuO_2 are currently the most suitable catalysts for the OER, while Pt is the most suitable for the hydrogen evolution reaction (HER). It is important to synthesize catalysts with good durability, high activation, low cost, high stability, and high energy efficiency [13, 20, 31, 47]. The catalyst must reduce the electrolyzer's operational overpotential, the additional potential needed to drive the chemical reaction at a specific rate, to achieve the market requirement durability specification and reduce the ohmic resistance of the system [49].

1.6 Problem statement

The PEMWE has many advantages over the AWE and SOWE, including higher energy efficiency, higher H_2 production rate, and a more compact system design [50]. However, the high cost of PEMWE components, including the anode catalyst, hinders the widespread commercialization of the technology. The anode catalyst was investigated because the anode has the highest overpotential in the system. A catalyst with higher OER activity and stability will result in other advantages [42], such as:

- Higher energy efficiency
- Longer lifetime
- Higher production capacity
- Lower noble metal quantities
- Cost reduction

1.7 Aims and Objectives

The IrO_2 catalyst is the most popular catalyst for the OER because of its very high stability. However, the OER activity of the IrO_2 needs to be improved to reduce the required metal loading. The study aims to synthesize the IrO_2 catalyst with improved OER performances. Improved results will reduce the use of high cost Ir precursors. This will reduce the high cost associated with the PEMWE and encourage the commercialization of the technology.

The objectives of the study were the following:

1. To use the modified Adams fusion method (MAFM) and the molten salt method (MSM) to prepare IrO_2 catalysts.

2. To optimize the IrO_2 catalyst preparation conditions to improve the catalyst OER activity and stability.

3. To physically characterize the IrO_2 catalysts with the X-ray diffractometer (XRD), High-resolution transmission electron microscopy (HRTEM), and the Brunauer-emmet-teller (BET).

4. To evaluate the performance of the IrO_2 catalysts using the Cyclic voltammetry (CV), Linear sweep voltammetry (LSV), and the Chronopotentiometry (CP).

5. To compare the synthesized IrO_2 catalysts with the commercial IrO_2 catalyst for benchmarking.

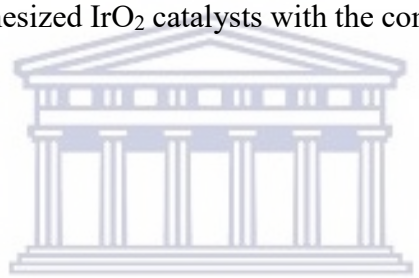

Chapter 2: Literature review

2.1 PEMWE features

The production of H_2 from H_2O using the PEMWE has gained much attention. The success of commercial PEMWE depends on its high performance, durability, and cost-effectiveness [51]. To make further improvements, it is important to study both the positive and negative features of PEMWE.

2.1.1 Positive features

The thin proton exchange membrane (PEM) can produce a proton conductivity of 0.1 ± 0.02 Scm^{-1} [20, 43]. The gas reduction in the electrodes is done by removing the synthesized gas according to Fick's law of diffusion. Low gas crossover rates synthesize H_2 with higher purity. This allows the PEMWE to operate at the entire nominal power density range while transporting the protons at a fast rate, without the delay of inertia. The PEMWE has good structural properties, a compact system design, and high operational pressures when using a solid electrolyte [28, 43]. Some commercial PEMWE can operate at 350 bar pressure [30, 51]. At high operational pressures, less energy is required for further H_2 storage and compression [28]. Furthermore, the integrity of the catalytic layer is maintained while the expansion and dehydration of the membrane are minimized [42]. Only the cathodic component of the PEMWE system is under pressure, eliminating the dangers of operating pressurized O_2 gas [11]

2.1.2 Negative features

The high operational pressures of PEMWE increase both the system pressures and the gas cross-permeation effect [28, 44]. To maintain an internal gas pressure above 100 bar, a thicker membrane is required [30]. When using membranes that are too thick, the anodic electrode produces an ionic resistance and overpotential [28, 41, 47]. When using a thinner membrane, the gas cross-permeation effect increases with higher operational pressures. The addition of different fillers inside the membrane is required to lower the membrane porosity [30, 42].

The PEMWE anodic catalyst needs to be synthesized with distinct materials to withstand the acidic nature of the PEM. Only scarce and expensive noble metals i.e., Ir, Ru, and Pt can resist the harsh acidic environment of the commercial Nafion® membrane [24, 29, 30, 42, 46]. Noble metals can be found in only a few countries. The Ir-metal

can be found in countries like Canada, Russia, and South Africa as pentlandite, sulfide ore laurite, and pyroxenite, respectively [30]. The Ru-metal can be found in North and South America, and South Africa in ural mountains, and pyroxenite deposits, respectively. The Pt-metal can be found in Colombia, South Africa, Russia, and Canada in ural mountains, and sperrylite [52]. It becomes vital to improve the catalytic performance of these scarce materials because it will decrease the catalytic metal loading whilst increasing the cost associated with PEMWE.

2.2 PEMWE electrode reactions

For the PEMWE reaction to occur the thermodynamic potential difference between the anodic and cathodic electrodes is provided. In theory, the potential difference occurs at +1.23 V vs. RHE, and in practice, the potential difference ranges between 1.3-2.0 V vs. RHE. The ohmic voltage losses and the polarization at the electrodes hinder the reaction from taking place at the theoretical value. When an ample potential difference is applied, the cathodic (H_2O reduction) and anodic (H_2O oxidation) reactions occur simultaneously on the electrodes, respectively. At the cathode, the electrons from the external circuit and the protons in the PEM are used to synthesize the H_2 gas. The process is known as the HER. At the anode, the OH^- ions are oxidized into O_2 gas and this process is known as the OER [42].

2.2.1 Hydrogen evolution reaction

The HER is the most studied electrochemical reaction. When compared to the OER, the HER is a more kinetically feasible reaction with only two steps involved [46]. The first reaction step is called the Volmer pathway and during the process the H^+ ions are bonded to the electrode adsorption sites. The second reaction step can occur either via the Tafel pathway or the Heyrovsky pathway [29, 46, 53]. If one of the steps turns into the rate determining step (RDS), the slowest step in the process, their associated Tafel slopes can be determined [46, 35]. Table 2.1 summarizes the different HER steps with their related Tafel slopes [53, 54].

Table 2.1: HER pathways with the respective Tafel slopes.

Path	Reaction step (rds.)	b_a at low η	b_a at high η
Volmer	$S + H^+ + e^- \leftrightarrows S—H_{ads}$	120	120
Heyrovsky	$S—H_{ads} + H^+ + e^- \leftrightarrows S + H_2$	40	120
Tafel	$2S—H_{ads} \rightarrow 2S + H_2$	30	∞

The bond strength (ΔH_t°) between the chemisorbed H (S-H) and metal surface determines the suitable catalyst for the reaction [55]. Catalytic metals with intermediate bond strength have the highest activity for the HER and hydrogen oxidation reaction. Lower activities are shown for catalytic metals with bond strengths that are too weak or too strong. When Pd or Pd based catalytic materials are used, the HER competes with the hydrogen insertion reaction to generate additional reaction steps [20, 36, 46]. The Pt catalyst allows a fast proton discharge, followed by the rate determining chemical desorption [46]. The metal loading of Pt for the HER is about 0.5 mgcm^{-2} [42]. A higher electron conductivity and corrosion resistance are obtained when using a carbon supported Pt as an alternative [30, 46]. Greeley et al. [56] experimentally confirmed the increased performance of BiPt surface alloy at pH 0. Figure 2.1 shows a Volcano shaped plot relating the exchange current density to the catalytic metal hydrogen bond strength [57, 58].

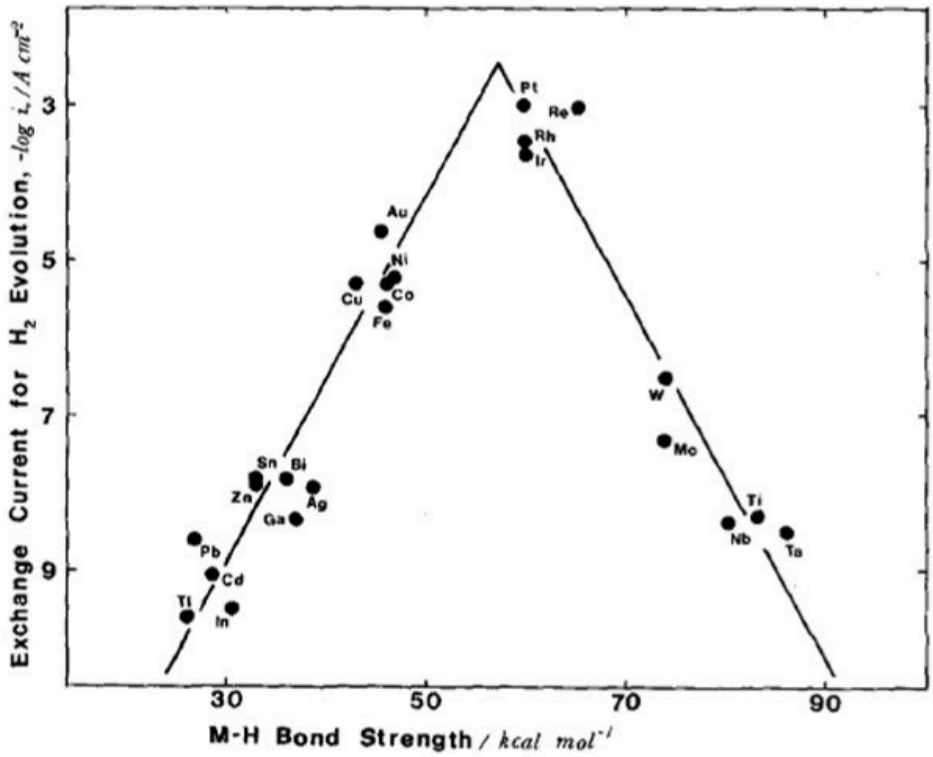

Figure 2.1: Volcano plot of HER exchange current density vs. bond strength.

2.2.2 Oxygen evolution reaction

The OER consists of three main mechanisms including the electrochemical oxide path, oxide path, and Krasil Shichikov path [46, 59]. Table 2.2 summarizes the different reaction steps with associated Tafel slopes, where S represents the catalytic surface-active sites, and S-O_{ads} and S-OH_{ads} represent the adsorption intermediates [35, 60, 61].

Table 2.2: OER pathways with respective Tafel slopes.

Path	Reaction step (rds.)	b_a at low η	b_a at high η
Electrochemical Oxide path	$S + H_2O \leftrightarrows S{-}OH_{ads} + H^+ + e^-$	120	120
	$S{-}OH_{ads} \leftrightarrows S{-}O + H^+ + e^-$	40	120
	$2S{-}O \rightarrow 2S + O_2$	15	∞
Oxide path	$S + H_2O \leftrightarrows S{-}OH_{ads} + H^+ + e^-$	120	120
	$2S{-}OH_{ads} \rightarrow S - O + S + H_2O$	30	∞
	$2S - O \rightarrow 2S + O_2$	15	∞
Krasil Shichikov	$S + H_2O \leftrightarrows S{-}OH_{ads} + H^+ + e^-$	120	120
	$S{-}OH_{ads} \rightarrow S - O^- + H^+$	60	60
	$S - O^- \rightarrow S - O + e^-$	30	120
	$2S - O \rightarrow 2S + O_2$	30	∞

In 1967, most OER catalysts were based on the dimensionally stable anode (DSA) electrode, which was invented by Beer [62]. Either a monometallic or bimetallic oxide (AO_x and/or BO_y) can be coated on a suitable base metal. The weaker oxygen-oxygen (O-O) bonds from the metal oxide catalysts allow the OER to occur on the oxide surface of the catalyst. The unique bonds between the oxygenated species and the metal surface change the oxidation state of the metal [59, 63]. Non-noble metals including Mn, Ni, Co, etc. cannot be used in the PEMWE because the metals corrode in the PEM acidic environment [20, 35]. Furthermore, the non-noble metal cations reduce the membrane conductivity by poisoning the membrane with sulfonic acid [35]. Supported materials like boron carbide, titanium carbide, and tantalum borde can be used to enhance the catalyst performance, however, higher cost is associated with supported catalysts [35]. PGM oxides like IrO_2 and RuO_2 were found to be the most stable catalysts for the OER. Even with the high cost associated, PGM oxides are the most common catalyst used for the OER due to their higher activities [35]. Both IrO_2 and RuO_2 catalysts show intermediate bond strength with good chemical stability and electronic conductivity [20, 29, 35, 64, 35]. The IrO_2 loading on the electrode is about 2 $mgcm^{-2}$, confirmed by Ayers et al. [47]. Mixing the PGM oxides with a cheaper material (e.g., SnO_2) allowed a reduction in the capital cost of the catalyst. However, disadvantages including decreased

OER conductivity, larger particle size, and low homogeneity were obtained for these samples [30]. Figure 2.2 shows the Volcano shaped plot of different metal oxides, relating the bond strength with their catalytic activity [65].

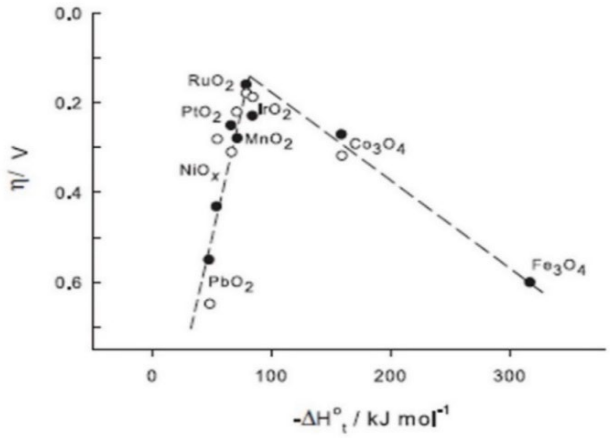

Figure 2.2: The OER activity of different oxides as a function of enthalpy transition.

2.3 Synthesis of IrO_2 catalyst

In the low overpotential-range, RuO_2 has a higher OER activity, but with lower stability [35]. The IrO_2 catalyst is known to be a 'state-of-the-art' catalyst for the OER [30]. IrO_2 is the most used, resistant, and stable catalyst in the PEMWE acidic environment when compared to RuO_2 [20, 35]. IrO_2 can also be used in field emission, sensing, electrical properties, and Li-air battery applications [66]. For these reasons, the IrO_2 catalyst was studied to further improve its OER performance i.e., the activity and stability.

Nanostructured IrO_2 is highlighted as the most favourable material to improve the OER activity of the anode electrode [66]. Arico et al. [35] showed how the characteristics and performance of the IrO_2 catalyst can be controlled by changing the reaction conditions. The methods and materials used to synthesize the catalyst are essential in obtaining increased PEMWE performances [30]. The IrO_2 stoichiometry, morphology, crystallinity, and electronic conductivity depend on the preparation techniques [67]. The IrO_2 catalyst can be synthesized using different techniques including the electrochemical synthesis, hydrothermal technique, vapor phase transport process, oleyl-amine-mediated synthesis, wetness technique, arc vaporization, precursor thermal

decomposition, sol-gel method, reactive radio frequency magnetron sputtering, sulfite complex route, etc. [28, 66, 67]. Many of the techniques are complex, expensive, not environmentally friendly, and use unstable Ir precursors. Other disadvantages associated with the abovementioned techniques include the complicated experimental set-ups and tedious synthesis procedures. This hinders both the economic and technical factors for the upscale of the IrO_2 catalyst. In the study, the MAFM and MSM were used to synthesize the IrO_2 catalysts. These techniques are simple, stable, cost-effective, and eco-friendly [66, 68]. A brief overview of the MAFM and MSM is presented in the sub-sections below.

2.3.1 Modified Adams fusion method

In 1923, Roger Adams and Ralph Shriner introduced the Adams fusion method for the preparation of PtO_2 [68, 69]. Today, the modified version of the Adams fusion method is used to synthesize different metal oxides i.e., IrO_2, RuO_2, and NiO_x [30]. Advantages associated with the MAFM include its simplicity, scalability, and easily removable NaCl salt by-product [70]. During the procedure, the H_2IrCl_6 precursor is mixed, as indicated by the stoichiometry, with a suitable solvent (i.e., H_2O, isopropanol, or mixture) [30, 71]. Under constant stirring, the finely ground $NaNO_3$ reagent is then added. The second metal precursor/support is included before the addition of $NaNO_3$ when producing bimetallic and supported catalyst [30]. At 70℃, the solvent is slowly evaporated. The dried mixture is further reacted at temperatures ranging between 400-500℃ to synthesize the metal oxide. The chemical reactions of the abovementioned procedures are shown in Equation 20 [30, 68, 70]. The NaCl salt is formed only after the calcination step and can be removed by washing the sample with 2 L deionized H_2O. The sample is then filtered and dried to produce the IrO_2 catalyst, as shown in Equation 21 [30, 70].

$$H_2IrCl_6 + 6NaNO_3 \rightarrow 6NaCl + Ir(NO_3)_4 + 2HNO_3 \quad (20)$$

$$Ir(NO_3)_4 \rightarrow IrO_2 + 4NO_3 + O_2 \quad (21)$$

Rasten et al. [72] studied the effect annealing temperatures had on the synthesized IrO_2 catalyst. When heat treating the sample at 340℃, different catalytic and electronic

properties were seen for IrO_2. At non-annealing temperatures, the HRTEM analysis showed low crystalline nanosized IrO_2 particles. The non-annealing IrO_2 also showed a low electronic conductivity with high catalytic activity. When increasing the annealing temperatures between 440-540℃, the IrO_2 becomes more crystalline with increased particle sizes. The electronic conductivity also increased while both the catalytic activity and active surface area decreased. When combining the polarisation and electrochemical impedance spectroscopy (EIS) curves, the reaction mechanism followed the electrochemical oxide path.

Zhang et al. [73] studied the effect the synthesized temperature, duration, and reagent mixture composition had on the production of SnO_2 catalyst. The $SnCl_2.2H_2O$ precursor was fused with $NaNO_3$ reagent to synthesize SnO_2 nanoparticles. The HRTEM analysis showed a crystal size/particle size increase from 2.5 nm/2.9 nm to 8.4 nm/8.6 nm with reaction temperatures ranging between 300-600 ℃. At 400 ℃, since it showed SnO_2 with the highest performance, the synthesis duration was ranged between 0.5-5 hrs. The crystal size/particle size increased from 2.3 nm/2.7 nm to 6.8 nm/7 nm, respectively. The mole ratio for the mixture combination $NaNO_3/SnCl_2.2H_2O$ was between 5-50, and the crystal size/particle size decreased from 7.8 nm/8.0 nm to 4.2 nm/4.3 nm. The experiments demonstrated that a 100% yield can be obtained when $SnCl_2.2H_2O$ is reacted with an excess of $NaNO_3$ at 400 ℃ for longer than an hr. The mixture combination $NaNO_3/SnCl_2.2H_2O$ that synthesized the highest performing IrO_2 was not specified.

Liu et al [74] studied the calcination temperatures, $NaNO_3$ reagent content, and different solvent effects on the synthesized IrO_2 catalyst. At 500 ℃, the highest specific surface area for the IrO_2 was obtained. Whereas the highest OER activity was obtained at calcining temperature 550℃. Three different weight ratios for H_2IrCl_4:$NaNO_3$ were chosen, including 1:10, 1:20, and 1:30. The IrO_2 catalyst with the highest OER activity and surface area was synthesized at a weight ration 1:20. The solvents studied were H_2O, alcohol, and isopropanol. The IrO_2 synthesized with H_2O showed the highest OER activity. The best performing IrO_2 catalyst showed increased OER performance at about 90 $mAcm^{-2}$ with an electrochemical surface area of about 126.4 m^2g^{-1}.

Cheng et al. [75] synthesized and compare the features of samples $Ir_{0.4}Ru_{0.6}O_2$ and $Ir_{0.4}Ru_{0.6}Mo_xO_y$. Both samples were doped for 1 min with Mo to generate their amorphous features. Sample $Ir_{0.4}Ru_{0.6}Mo_xO_y$ has a decreased particle size when combining Ir and Ru with Mo, which increased both the OER performance and the specific active surface area.

Polonsky et al. [76] studied the effect the presence of TaC support had on the production of IrO_2. About 50 wt.% or more IrO_2 was added to the synthesis of $NaTaO_3$ film to overcome its associated negative effect. Below synthesis temperatures of 200℃, the TaC support stabilized. A high number of nucleation centres were shown for the supported IrO_2 catalyst. When using a higher concentration of support, the IrO_2 catalyst showed larger crystallite sized particles. However, similar OER activity results were seen for both pure IrO_2 and supported IrO_2 catalysts. The obtained results were confirmed by testing the IrO_2 catalysts in a PEMWE under real water electrolysis conditions.

2.3.2 Molten salt method

The MSM is based on the use of an inorganic reagent as the medium for the reaction. The reagent usually has physicochemical properties like higher mass transfer, greater oxidizing potentials, lower densities, and higher thermal conductivity [77]. Other factors including the dissolution rate of the reagent, duration and heating of the precursor, chemical composition of the precursor, and the melting point of the reagent can influence the structural properties of the obtained samples [77, 78]. During the procedure, the Ir precursor decomposes on the NaCl/KCl salt bed. The NaCl/KCl salt bed does not chemically react with the Ir precursor but acts as a support for the thermal decomposition of the Ir precursor in air. The synthesis temperature is mostly kept at 650℃ which is below the melting point of the NaCl/KCl salt mixture [66]. The resulting sample is washed with 2 L deionized H_2O, vacuum filtered and dried in an air oven to produce the IrO_2 catalyst [66].

The advantages associated with the MSM include eco-friendliness, high stability, scalability, easily removable NaCl/KCl salt by-product, and cost-effectiveness [66, 77]. Low vapor pressures and chemical inertness are also related to the MSM. No surfactant or capping agent is involved during the reaction which allows the generation of products

with clean surfaces [67]. The MSM facilities allow a wide range of ternary metal oxides to be synthesized [77].

Ahmed et al. [66] synthesized ultrafine IrO_2 nanorods at a 650℃ temperature. A higher current density (~70 $mAcm^{-2}$ at 0.6 V vs. RHE) was seen for the synthesized IrO_2 when compared to a commercial IrO_2. The CV and chronoamperometry analysis show the enhanced OER and HER activities of the IrO_2 nanorods. After saturating the 0.5 M KOH electrolyte with O_2, an increased OER current density of 71 $mAcm^{-2}$ was obtained. Whereas the HER current density of the IrO_2 nanorods was found to be at 25 $mAcm^{-2}$.

Lim et al. [79] synthesized and studied ultrathin IrO_2 nanoneedles with the addition of cysteamine. Different amounts of cysteamine were added to control the aspect ratio of the obtained nanoneedle and unshaped IrO_2 particles. Both the nanoneedle and unshaped IrO_2 particles showed improved OER performances with enhanced electrical conductivities. At 450℃, unshaped IrO_2 had an enhanced mass activity of 51.6 Ag^{-1} oxide, whereas the IrO_2 nanoneedles had a mass activity of 15.5 Ag^{-1}. The IrO_2 nanoneedles were stable for more than 200 hrs at a current density of 2000 $mAcm^{-2}$. Other advantages associated with the IrO_2 nanoneedles include higher durability and efficiency when compared to the unshaped IrO_2 particles.

Zhou et al. [77] studied the effect reagent medium, annealing temperatures, cooling rates, duration, and precursor types had on the production of $BaZrO_3$ particles. Both the reactivity and solubility of the synthesized particle changed with the change in the reagent medium. At 820℃, the $BaZrO_3$ weight percentage increased from 69% to 93.6% in the presence of NaCl. In the presence of a 50:50 mol% ratio of NaCl/KCl, a 100% weight percentage for $BaZrO_3$ was obtained. In Cl-containing media, cubic shaped particles were formed, and in OH^--containing media, spherical shaped particles were formed. High quality $BaZrO_3$ particles were favoured with slow cooling rates, high annealing temperatures, and longer durations. At 720℃ with a heating rate of 5 ℃/min well-dispersed crystalline particles were synthesized. Small-sized cubic shaped particles were synthesized with shorter annealing duration i.e., 30 min. Annealing durations ranging between 60-210 min resulted in a change in particle shapes, from cubic to spherical particles or a mixture of both.

2.3.3 Conclusion

The high cost of the PEMWE can be reduced by selecting vital materials and methods for the synthesis of the IrO_2 catalysts [30]. The preparation technique can alter the IrO_2 crystallinity, morphology, stoichiometry, and electronic conductivity [67]. The different preparation techniques include the hydrothermal technique, electrochemical synthesis, vapor phase transport process, etc. [28, 66, 67]. However, many of these techniques are expensive, complex, and not eco-friendly. The IrO_2 catalyst in this study was synthesized using the MAFM and MSM. These methods are simple, scalable, and eco-friendly [66, 70, 77]. The MAFM and MSM can synthesize different products i.e., RuO_2 and NiO_2, with particle sizes in the nanosized range. Zhang et al. [73] used the MAFM to synthesize SnO_2. Whereas Cheng et al. [75] used the MAFM to synthesize bimetallic oxides i.e., $Ir_{0.4}Ru_{0.6}O_2$. High performance $BaZrO_3$, for fuel cell applications, can be synthesized using the MSM [77].

The difference in experimental procedures between the MAFM and MSM results in the production of different IrO_2 nanoparticles. For the MAFM, the IrO_2 is usually produced at temperatures ranging between 300-600℃ since the $NaNO_3$ reagent has a melting point of 308℃ [68]. Liu et al. [74] synthesized aggregated IrO_2 particles below 500℃. Whereas the MSM produces IrO_2 at increased temperatures ranging between 350-800℃ since the melting point of the NaCl/KCl salt bed is above 600℃. Lim et al. [79] synthesized a variety of IrO_2 nanoparticles when using the MSM, depending on the synthesis temperature. Optimizing the MAFM and MSM parameters, including the synthesis temperatures, reagent medium, synthesis duration, and metal precursors, allows the production of IrO_2 with improved OER performances for the PEMWE.

2.4 Physical characterization techniques

The IrO_2 catalysts synthesized with the MAFM and MSM were physically characterized using the (i) XRD, (ii) HRTEM, and (iii) BET technique. The techniques are discussed in the sub-sections below.

2.4.1 Theory of x-ray diffraction

The XRD analysis is a popular technique for the classification, both quantitatively and qualitatively, of crystalline materials. The fast, easy, and non-destructive material preparation for accurate results makes the XRD technique favourable [80]. Different

materials like metals, polymers, minerals, catalysts, semiconductors, ceramics, and pharmaceuticals can be analyzed using the XRD technique [80]. Information about the materials including their shape, distribution, composition, and purity is obtained [80, 81]. Crystals of the material with the same interatomic spacing and x-ray wavelength are classified as the same component [82]. The crystals act as a 3D diffraction grating when the material electrons interact with the x-ray, causing the electrons to oscillate in the incident x-ray frequency [83]. Consequently, radiation of oscillation frequency is emitted by the oscillating electrons [84]. The material electrons emit both constructive and destructive interferences, also known as the Thomson scattering. The x-ray diffraction patterns of the crystalline planes are shown in Figure 2.3 [11].

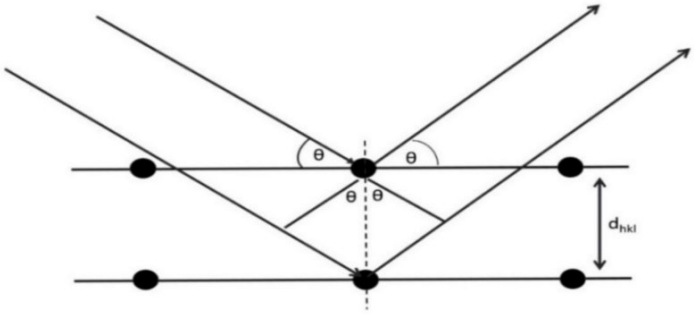

Figure 2.3: Bragg's reflection from a hkl crystal plane.

A constructive peak interference can be calculated by using the Bragg's reflection (Equation 22) [80].

$$2d_{hkl}\sin\theta = n\lambda \tag{22}$$

h, k and l are the spacing between Miller indices with the lattice planes. n gives the order of diffraction (e.g., 1, 2, 3, etc.), known as the wavelength of incident x-ray.

In an x-ray tube, the x-rays are synthesized by bombarding the tube with accelerating electrons generated from a heated tungsten filament. When struck by high-speed

electrons, the metal target's core level ejects electrons. A hole is then formed at the core level. Electrons in the upper-level travel to the core level to produce energy in the form of an x-ray. The sample being studied is bombarded with x-rays from different angles. A suitable detector is used to study the emitted rays, as shown in Figure 2.4 [11].

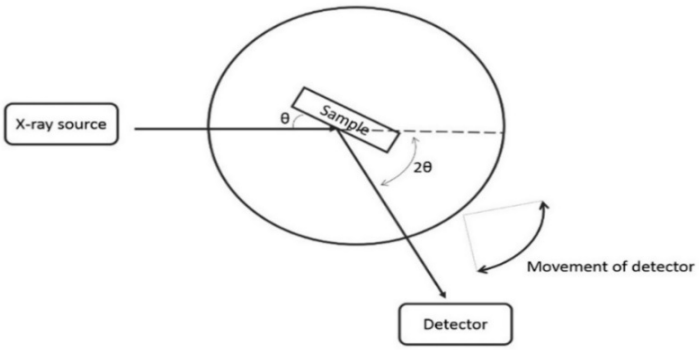

Figure 2.4: Basic XRD instrumental set-up.

Different materials generate different x-ray diffraction patterns that are unique to the sample [84]. The produced patterns are plotted on an angle vs. intensity graph, also known as an XRD graph [80]. Figure 2.5 shows the XRD graph of IrO_2 synthesized with the MSM at 650℃ for 12 hrs [66]. The JCPDS library is used to identify the material crystals by comparing the d-spacing and peak intensity. Broad XRD peaks are shown for partially crystalline and amorphous substances [85].

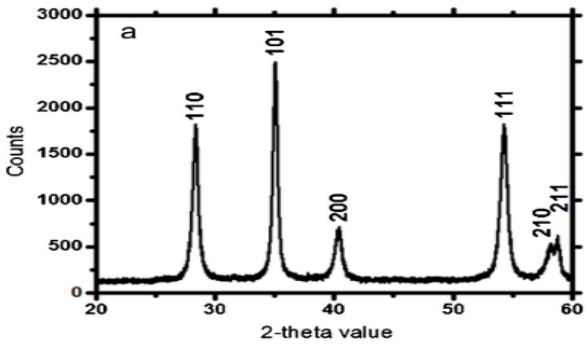

Figure 2.5: Powder XRD pattern of the IrO_2 catalyst synthesized using the MSM at 650℃ for 12 hrs.

The average crystallite size can be calculated using the broadness of the peak with the Debye-Scherrer formula, given in Equation 23 [84, 85].

$$d_p = \frac{K\lambda}{\beta \cos\theta} \tag{23}$$

where the incident x-ray wavelength is the full width at half maximum, and K usually has a value of 0.9 and is the shape factor if assumed the crystallite shape is spherical.

2.4.2 Theory of high-resolution transmission electron microscopy

The HRTEM provides information, on the nanoscale, about the orientation, separation distance, lamella size, and density between particles [86, 87]. Direct information at the atomic level of the material is provided. The HRTEM has similar basic principles to the SEM (Scanning electron microscopy) technique and is widely used in combination with the XRD [82, 86]. During the analysis, an electron beam transfer energy to the sample atoms using either a field or thermionic emission, as shown in Figure 2.6 [88, 89, 90].

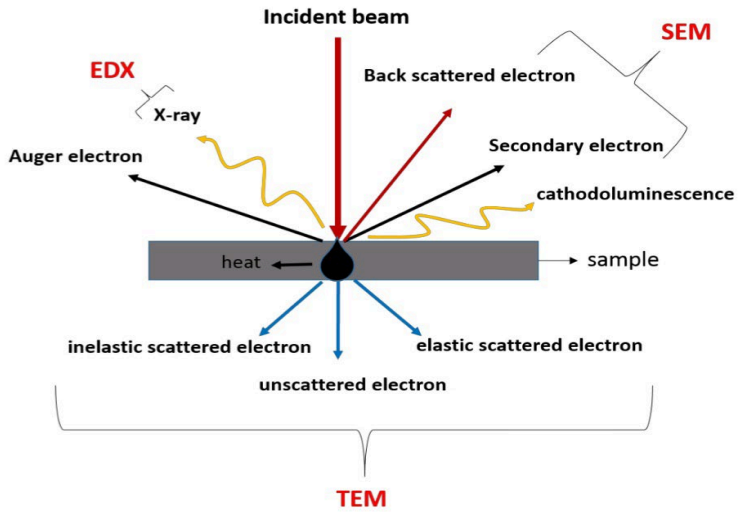

Figure 2.6: Different electron bombardment effects on a sample.

Three types of transmitted electrons are used in the study, i.e., unscattered, elastically scattered, and inelastically scattered electrons [90]. The electrons are emitted using

either field or thermionic emission. A lens system is used to image the elastic scattered and unscattered electron intensity as dark and light areas, which shows the structure of the sample. Elements with higher atomic numbers scatter more electrons as compared to elements with lower atomic numbers, creating different intensity regions. The sample images are digitally recorded using charge-coupled device (CCD) cameras [86, 89]. An image processing software is used to generate the HRTEM image, and the result is interpreted qualitatively [86]. The HRTEM image of the IrO_2 catalyst synthesized with the MSM at 650℃ for 12 hrs is shown in Figure 2.7 [66].

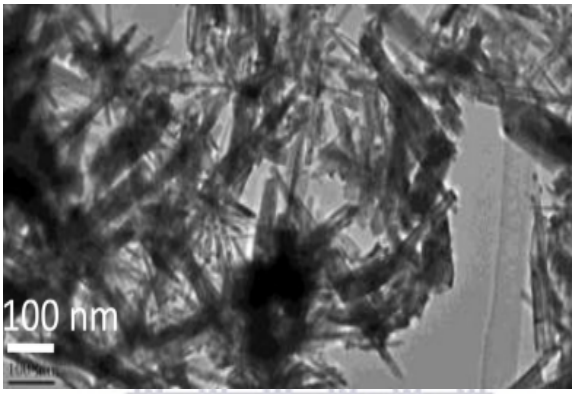

Figure 2.7: Typical HRETM image of IrO_2 synthesized with the MSM at 650℃ for 12 hrs.

2.4.3 Theory of Brunauer-emmet-teller

The BET technique is mainly used for solid surface area analysis of structure heterogeneity, pore size, and adsorbate-adsorbent interactions, using N_2 physical adsorption. Fundamentally, the BET technique is an empirical procedure that uses both theoretical assumptions and empirical parameters, including the adsorbed gas cross-section area. The materials studied with the BET technique are either crystalline metal, crystalline organic materials, or active amorphous carbon. It is ideal to study the abovementioned materials with large pore sizes as the BET technique studies the adsorption of uniform gas molecules with no lateral interaction. The BET surface area of porous material is determined from an adsorption isotherm linear fitting graph at 77 K^3 for N_2, as shown in Figure 2.8 [91, 92].

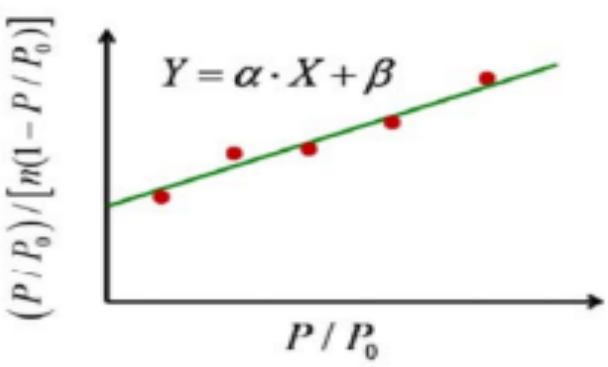

Figure 2.8: The linear fitting of gas adsorption amount in relation to pressure.

From the adsorption isotherm linear fitting graph, the volume of the gas needed to cover the monolayer surface area per unit mass is calculated using Equation 24 [91].

$$\frac{P/P_0}{n(1-P/P_0)} = \frac{1}{n_m k_0} + \frac{k_0 - 1}{n_m k_0} \cdot \frac{P}{P_0} \tag{24}$$

where P is the bulk phase gas pressure, P_o is the gas saturation pressure (the atmospheric pressure of the process that is above the N_2 boiling point), n is the volume of the gas adsorption per unit mass of the sample, n_m is the volume of the required gas to cover a monolayer surface per unit mass and k_0 is proportional to the lowered surface adsorption energy.

The BET surface area is calculated (Equation 25) by assuming the effective monolayer capacity, corresponding to the conditions, is completely covered with the gas molecules.

$$S_{BET} = n_m \cdot a^2 \tag{25}$$

where a^2 is the cross-sectional area of the N_2 in the monolayer and is equal to 0.162 nm^2 at 77 K[7].

2.5 Electrochemical characterization techniques

The electrochemical characterizations are carried out in a three-electrode cell. The potential is determined between the reference electrode (RE) and the working electrode (WE). The current density is determined between the counter electrode (CE) and the WE [93, 94]. The IrO_2 catalysts synthesized with the MAFM and MSM were electrochemically characterized using (i) CV, (ii) LSV, and the (iii) CP techniques. The techniques are discussed in the sub-sections below.

2.5.1 Theory of cyclic voltammetry

In 1938, Metheson and Nichols first introduced the CV technique. CV is a simple, fast, and the most straightforward technique to obtain information about the properties of different materials [94-96]. During the CV process, species P undergoes a reversible one-electron reduction to synthesize species Q, as shown in Figure 2.9 [97].

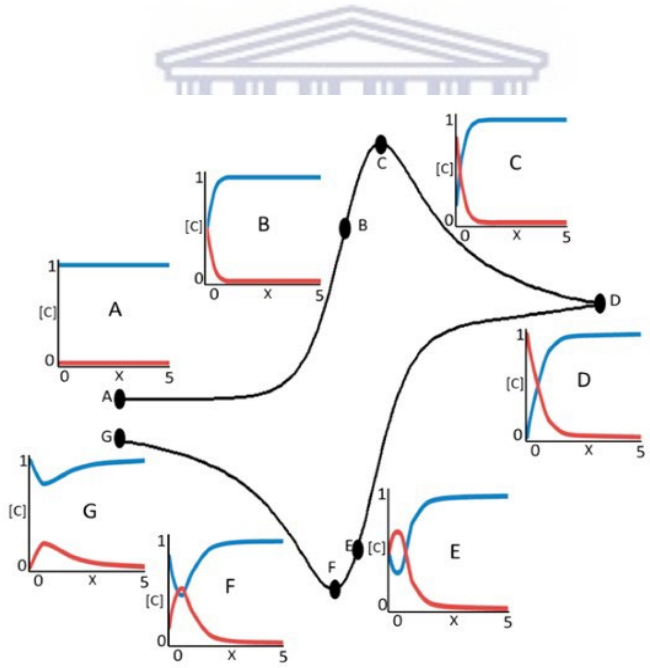

Figure 2.9: The concentration (C) versus distance (x) from the electrode at different points during a reversible CV wave; C_Q (red) and C_P (blue).

The CV initially starts at 0 V vs. RHE and proceeds in the negative scanning direction. A cathodic current starts to flow as the potential reaches a sufficiently negative value to reduce species P to species Q. Consequently, the electroactive species from the material

is transported, via diffusion, to the electrode surface. The electron transfer rate remains constant between the analyte and the electrode [94, 97]. The Nernst equation can be used to explain the change in the cathodic current (Equation 26) [95, 97, 98].

$$E = E^{\circ\prime} + \frac{RT}{nF} \ln\frac{CP}{CQ} \quad (26)$$

where C_P is the concentration of P, C_Q is the concentration of Q, and E°' is the reduction process formal potential.

The C_P and C_Q ratio changes when the applied potential changes. There is a fast increase in the cathodic current as species P decreases. This can be seen as a peak in the obtained cyclic voltammogram. For more current to flow, the oxidized species from the electrolyte must be transferred to the electrode surface. When the concentration of the unstirred solution and the electrolyte are very high, the diffusion rate instructs the current. At the reversed scan direction, when the potential switches, the current flow continues. At this point, the thickness of the diffusion layer has increased while the concentration of the electrode species has decreased. The same principles are followed for the anodic current flow as positive potentials are applied. The concentration reduction of species P correspond to the increased concentration of species Q [94, 97].

The obtained cyclic voltammogram is also known as the current vs. potential graph [94]. A typical metallic catalyst profile has several characteristic anodic and cathodic peaks. The IrO_2 CV shows various characteristic features with well-distinct peaks in the double layer region [95]. Figure 2.10 shows the IrO_2 characteristic peaks, including the redox transition of Ir(III)/Ir(IV) and Ir(IV)/Ir(VI) at ~0.75 and ~1 V vs. RHE, respectively [99-101].

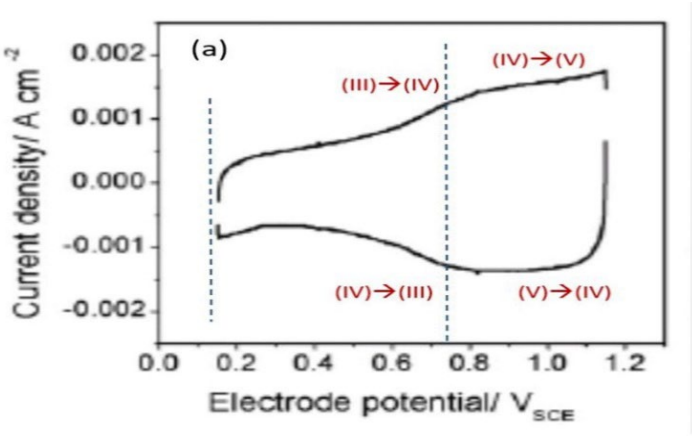

Figure 2.10: Typical IrO_2 CV in a 0.5 M H_2SO_4 solution.

2.7.2 Theory of linear sweep voltammetry

The LSV technique is used to study the electrochemical activity of the catalyst by measuring the overpotential of the sample [102]. The Tafel slopes for the catalyst can also be determined using the LSV technique. The Tafel slopes show the quality of the catalyst. More active catalysts show a lower Tafel slope, under constant catalytic conditions [103]. During the LSV experiment, as shown in Figure 2.11, the current responds start at the activation potential (Ea). The value of Ea relates to the onset energy where the electrochemical reaction occurs. The electroactive species continues to deplete near the surface electrode as the potential shifts from Ea to the peak potential (Ep). At the Ep, the reactive electrochemical species has fully transformed and the current response decreases beyond this point [104, 105].

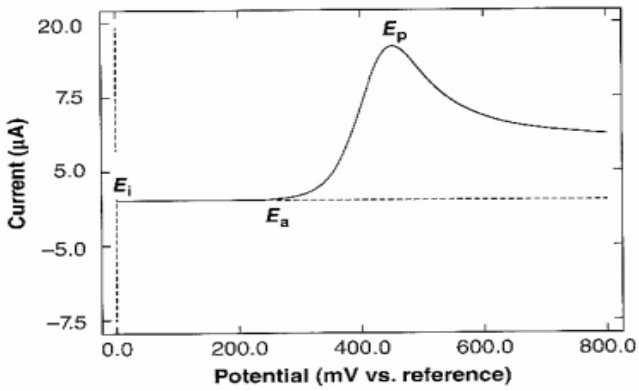

Figure 2.11: Typical experimental LSV response.

From the LSV graph, the overpotential can be calculated by subtracting the catalyst operational potential from the reaction equilibrium potential at a specific current density (Equation 27) [49, 97, 106, 107]. The value of the potentials can change but the determination of the overpotentials stays the same [49]. The operational potentials of different catalysts are determined at 10 $mAcm^{-2}$. This current density relates to the solar-to-hydrogen (STH) efficiency of 12.3%, which produces high catalytic performance in sufficient water-splitting technologies [108].

$$\eta = |E° - E_{cat/2}| \quad (27)$$

where η is the overpotential, E° is the equilibrium potential, and $E_{cat/2}$ are the operational catalytic potential.

2.7.4 Theory of chronopotentiometry

The CP is an electroanalytical technique to study the stability of electroactive species in an electrolyzer [109, 110]. CP analysis has the same accuracy as classical polarography however, the only difference is the higher sensitivity and adaptability of CP to a sample [111]. Another advantage is the ohmic effect correction when a constant potential offset is applied to the electrochemical processes. During the CP experiment a constant current density, 10 $mAcm^{-2}$, is applied to both the WE and RE, allowing the WE surface kinetics to be studied as a function of time [110-112]. As the chemical reaction proceeds, a depletion of the active species can be seen at the WE which may be caused by the samples' degradation. The results obtained from the CP can be seen in the potential-time graph, as shown in Figure 2.12 [109].

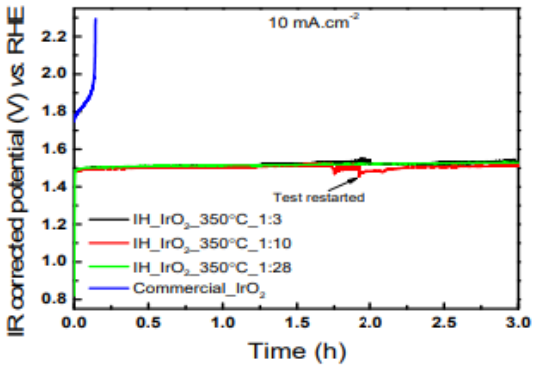

Figure 2.12: Typical IrO_2 CP in a 0.5 M H_2SO_4 solution at 10 $mAcm^{-2}$.

Chapter 3: Experimental

3.1 Chemicals and apparatus

The chemicals used to synthesize the IrO_2 catalyst, and to prepare and test the WE are shown in Table 3.1, 3.2, and 3.3 respectively.

Table 3.1: Chemicals used to synthesize IrO_2 catalysts.

Chemicals	**Supplier**
H_2IrCl_6	Alfa-Aesar (United States)
$NaNO_3$	Alfa-Aesar (United States)
Isopropanol	Alfa-Aesar (United States)
KCl	Laborem Lab Supplies (South Africa)
NaCl	Laborem Lab Supplies (South Africa)
IrO_2 commercial	Alfa-Aesar (United States)

Table 3.2: Chemicals used to prepare the anode.

Chemicals	**Supplier**
Nafion® Solution 5 wt %	Alfa-Aesar (United States)
Isopropanol	Alfa-Aesar (United States)
Ultrapure H_2O *	In-house

*Ultrapure H_2O was obtained using Milli-Q® ultrapure H_2O system and the H_2O resistance was 18.3 MΩ.cm.

Table 3.3: Apparatus used during electrochemical analysis

Magnetic stirrer and hotplate	DragonLab
Waterbath	Scientific Manufacturing cc.
Oven with electrical heating	Binder GmbH
Ultrasonic homogenizer	BioLogics Inc
Muffle furnace with electrical heating	Kiln contracts (Pty) Ltd.
PGSTAT302N Potentiostat/Galvanostat	Metrohm (Pty) Ltd.
Working electrode	Metrohm (Pty) Ltd.
Counter electrode	Metrohm (Pty) Ltd.
Reference electrode	Metrohm (Pty) Ltd.

3.2 IrO_2 catalyst synthesis

3.2.1 Modified Adams fusion method

An amount of 800 mg H_2IrCl_6 precursor was dissolved in 15 mL isopropanol and magnetically stirred for 30 min, at 300 rotations per minute (rpm). Finely ground $NaNO_3$, or KNO_3, was added to the mixture and stirred for another 30 min. Then the isopropyl was evaporated from the mixture on a hotplate and further dried in an oven, for 15 min at 85℃. The dried mixture was cooled and transferred to a porcelain crucible. The synthesis duration was constant at 2 hrs while the temperatures were 350, 500, and 650 ℃. The obtained metal oxide was filtered four times with 500 mL of Milli-Q ultrapure H_2O to remove the unreacted salts. A 0.1M $AgNO_3$ solution was used to ensure no chloride was present in the filtrate of the last 500 mL ultrapure water filter. In the final step, the IrO_2 was dried at 85℃ for 2 hrs and cooled inside the oven overnight. A commercial IrO_2 was used for comparison purposes and the synthesized IrO_2 are presented in the format Method-Temperature-Time-Salt, e.g., MFAM-350-2-$NaNO_3$. A simplified schematic of the MAFM for the synthesized IrO_2 catalyst is shown in Figure 3.1.

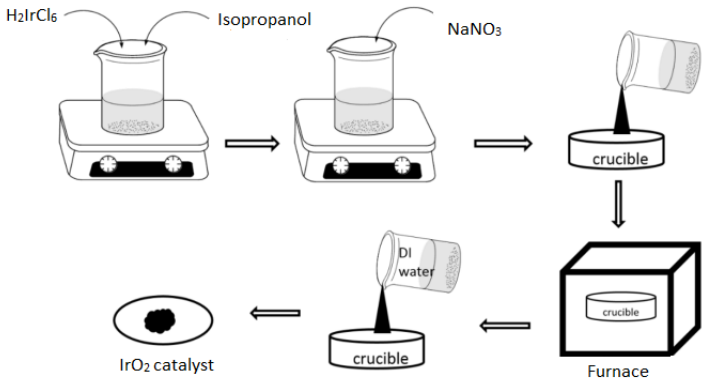

Figure 3.1: Simplified schematic of the MAFM for the synthesized IrO_2 catalyst.

3.2.2 Molten salt method

An amount of 400 mg H_2IrCl_6 precursor and 15000 mg NaCl were grounded together for 15 min. Then the mixture was transferred to a crucible and reacted in a furnace. The reaction times were varied between 4 and 8 hrs and the temperatures were 350, 500, and 650℃. The sample was left to cool overnight in the furnace and filtered six times with 500 mL Milli-Q ultrapure H_2O to remove unreacted chloride salt. A 0.1M $AgNO_3$ solution was used to ensure no chloride was present in the filtrate of the last 500 mL ultrapure water rinse. In the last step, the metal oxide was dried at 85℃ for 4 hrs and left to cool overnight in the oven. A commercial IrO_2 was used for comparison purposes and the synthesized IrO_2 are presented in the format Method-Temperature-Time-Salt, e.g., MSM-350-4-NaCl. The simplified schematic of the MSM for the synthesized IrO_2 catalysts is shown in Figure 3.2.

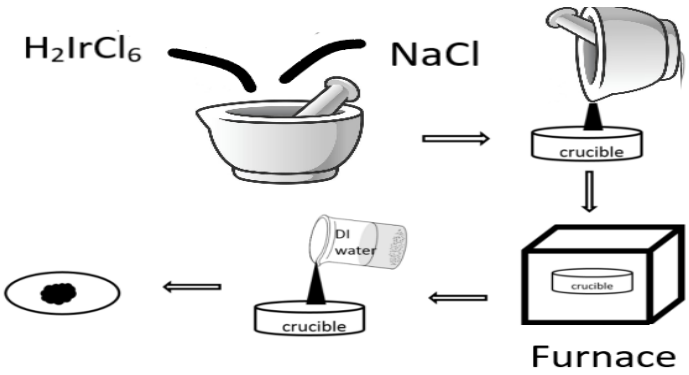

Figure 3.2: Simplified schematic of the MSM for synthesized IrO_2 catalyst.

3.3 Preparation of the working electrode

All electrochemical measurements were performed using a 0.196 cm^2 area glassy carbon electrode as the WE. The glassy carbon electrode was cleaned with 0.05 µm alumina paste, polished and treated in an ultrasonic H_2O bath to remove any surface particles before use (Figure 3.3). Elgrishi et al. [113] show how the glassy carbon electrode was polished and cleaned.

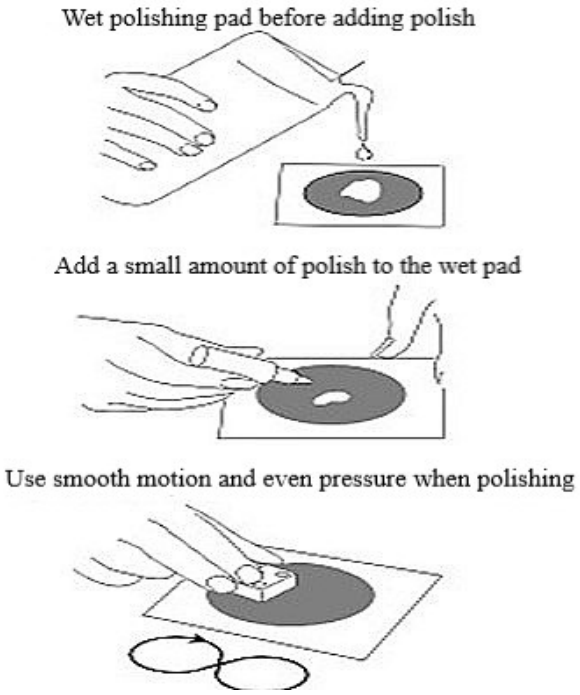

Figure 3.3: Polish and cleaning of the glassy carbon WE.

The IrO_2 catalyst ink was prepared, as shown in Figure 3.4, by dispersing 8 mg IrO_2, 50 μL Nafion solution (5 wt%), and 1950 μL Milli-Q ultrapure H_2O using an ultrasonic homogenizer for 15 min. About 30 μL, which equates to 0.61 $mgcm^{-2}$, IrO_2 catalyst ink loading, was deposited on the glassy carbon WE with a micropipette. The ink was then air dried overnight at ambient air before studying the IrO_2 electrochemical characteristics.

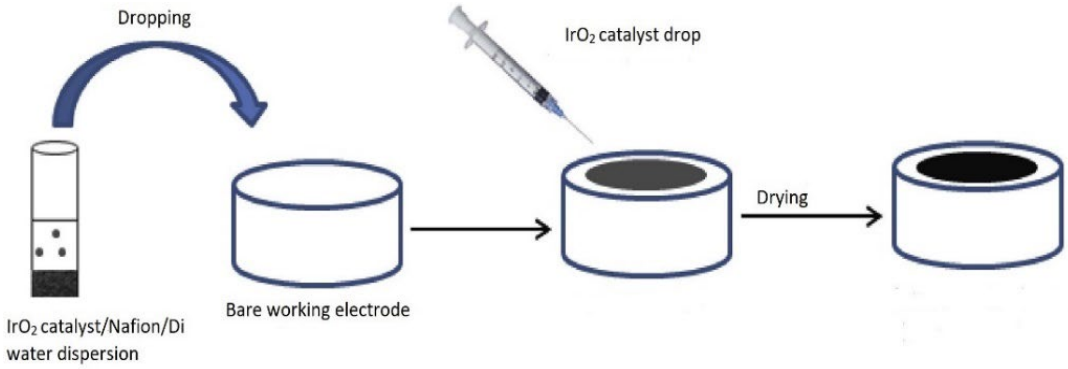

Figure 3.4: IrO_2 catalyst ink preparation.

3.4 Physical characterization

3.4.1 X-ray diffraction

The x-ray diffractometer D8-advance with Cu-Kα radiation from Bruker was used to investigate about 40 mg metal oxide. The data evaluation was done with EVA software from Bruker.

Table 3.4: The specification of the D8-advance XRD measurements.

Tube current	40 mA
Tube voltage	40 kV
Variable slits	V20
Increments Δ2θ	0.034°
Measurement time	0.5 s/step
2θ Range available	0.5-130°
Temperature	25℃

The x-ray diffractometer D2-advance with Cu-K Kα radiation (I=1.5418 A) from Bruker was used to also investigate about 40 mg metal oxide. The EVA software from Bruker was used to evaluate the data.

Table 3.5: The specification of the D2-advance XRD measurements.

Tube current	10 mA
Tube voltage	30 kV
Variable slits	V20
Increments Δ2θ	0.02°
Measurement time	0.5 s/step
2θ Range available	4-80°
Temperature	25℃

3.4.2 High-resolution transmission electron microscopy

The HRTEM analysis was performed using the FEI Tecnai G2 F20 S-Twin and operated at 200 kV. The sample preparation involved sonicating 10 mg IrO_2 with absolute ethanol for a few minutes. A few drops of the dispersion were then left to dry on a carbon-coated copper grid for analysis.

3.4.3 Brunauer-emmet-teller

The weighing of the metal oxide and specific test tube design is an important step in the preparation of the BET analysis. Test tubes containing about 100 g of IrO_2 were placed in the Micromeritics Flowprep TM 060 oven apertures. The IrO_2 catalysts were then degassed with a low nitrogen gas flux, 20 cm^3min^{-1}, at 130℃ for 24 hrs to remove physiosorbed H_2O. Next, the test tubes were mounted to the Micromeritics 3 Flex to study the surface area of the IrO_2. Liquid nitrogen, with a bath temperature of -196.15℃, was used for the adsorptive analysis.

3.5 Electrochemical characterization

All the electrochemical characterization was performed at 25℃ and 1 atm using an Autolab potentiostat PGSTAT302N. The glassy carbon WE (described in 3.3), a 3M Ag/AgCl RE, a 1 Pt sheet (1 cm^2 area) CE, which is 5 times large than the WE, and a 0.5 M $H_2SO_{4(aq)}$ electrolyte were used. Potentials were converted from the 3M Ag/AgCl electrode to the RHE by adding 0.21 V to all measured potentials [106]. The current was reported to current density by converting the surface area of the WE to 1 cm^2 by diving the current measured with the geometric surface area of the glassy carbon electrode. The

electrolyte was purged with N_2 for 15 min before performing electrochemical measurements. Electrode activation was performed via CV cycling in the potential window 0 to +1.4 V vs. RHE at a potential scan rate of 20 mVs^{-1} for 50 cycles before conducting any electrochemical characterizations. The electrochemical measurement set-up used during the study is shown in Figure 3.5.

Figure 3.5: The electrochemical measurement set-up.

3.5.1 Cyclic voltammetry

Table 3.6: The specification of the CV measurements.

Start potential	0 V vs. RHE
Upper vertex current density	+5 $mAcm^{-2}$
Lower vertex current density	-5 $mAcm^{-2}$
Highest current range	100 mA
Lowest current range	100 nA
Number of scans	2
Scan rate	0.2 Vs^{-1}

3.5.2 Linear sweep voltammetry

Table 3.7: The specification of the LSV measurements.

Start potential	0 V vs. RHE
Stop potential	1.8 V vs. RHE
Scan rate	0.002 Vs^{-1}
Current range	100 mA
Rotation rate of WE	1600 rpm

3.5.4 Chronopotentiometry

Table 3.8: The specification of the CP measurements.

Current range	1 mA
Rotation rate of WE	1600 rpm
Cut off max voltage	1.8 V vs. RHE
Interval time	5 sec

Chapter 4: Results and Discussion

4.1 Modified Adams fusion method

4.1.1 Effect of reagents on the IrO_2 catalyst

The optimization of the MAFM preparation conditions is essential to produce IrO_2 with improved OER activity and stability. To study the effect the reagents $NaNO_3$ and KNO_3 had on the IrO_2 performance, the synthesis duration (2 hrs) and temperature (350℃) remained constant. The XRD spectra of the commercial IrO_2 and the IrO_2 synthesized with the MAFM when using different reagents are shown in Figure 4.1. The peaks were assigned using the JCP2 standard files for IrO_2 (JCP2_150870) and Ir (JCP2_06-0598). Broad peaks can be seen for both MAFM-350-2-$NaNO_3$ and MAFM-350-2-KNO_3 which indicate their amorphous nature. Smaller particle sizes are usually in the amorphous phase [114]. The (101) facet, which is an important stable facet for IrO_2, was present in both MAFM-350-2-$NaNO_3$ and MAFM-350-2-KNO_3. The MSM-350-2-NaNO3 had a higher crystallinity due to the presence of the (211) facet at ~57°. A similar observation of increased crystallinity with a change in reagent was made by Zhou et al. [94]. The commercial IrO_2 showed an overlap of IrO_2 and Ir at the *Bragg* angles of ~69°. At the *Bragg* angle ~ 41° and ~ 47°, metallic Ir was present for the commercial IrO_2. The presence of metallic Ir in the catalysts may negatively affect the OER performance [73].

The average crystallite sizes were determined using the Scherrer formula as shown in Equation 23, at (101) facet. The (101) facet is preferred since it is a closed-packed Ir atom plane [68]. Table 4.1 summarizes the estimated crystallite sizes of the IrO_2 catalysts. The crystallite sizes of MAFM-350-2-$NaNO_3$ are larger than the crystallite sizes of MAFM-350-2-KNO_3. The difference in IrO_2 crystallite sizes between the two samples may be due to the precursor diffusion of $NaNO_3$ and KNO_3, decomposition of $NaNO_3$ and KNO_3, the reaction of the precursor with $NaNO_3$ and KNO_3, and the formation of the metal oxide between $NaNO_3$ and KNO_3 since the melting point of $NaNO_3$ is at 308℃ and for KNO_3 it is at 380℃ [70]. Puthiyapura et al. [70] also suggest that a smaller crystallite size may not necessarily lead to enhanced electrochemical activity due to different associated factors, including diluting the metal oxide. However, the commercial IrO2 does not show any crystallite size at the (101) facet.

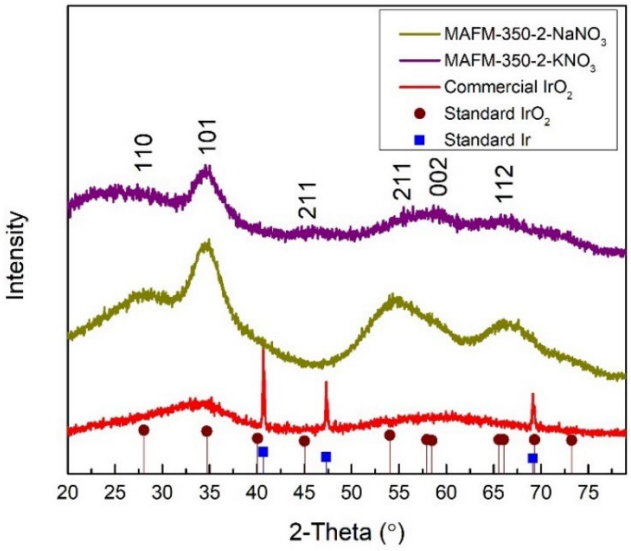

Figure 4.1: XRD analysis of the commercial IrO_2 and IrO_2 synthesized using the MAFM with $NaNO_3$ and KNO_3.

Table 4.1: Average crystallite sizes calculated using the Scherrer equation of the commercial IrO_2 and IrO_2 synthesized using the MAFM with $NaNO_3$ and KNO_3.

Sample name	IrO_2 Crystallite Size (nm) by Scherrer formula
MAFM-350-2-$NaNO_3$	2.73
MAFM-350-2-KNO_3	2.41
Commercial IrO_2	0

HRTEM analysis was used to study the morphology of MAFM-350-2-$NaNO_3$ and MAFM-350-2-KNO_3. Both MAFM-350-2-$NaNO_3$ and MAFM-350-2-KNO_3 showed well-dispersed uniform spherical particles that are less than 5 nm (Figure 4.2A and Figure 4.2C). The selected area electron diffraction (SAED) image in Figure 4.2B and Figure 4.2D, confirmed the amorphous nature of MAFM-350-2-$NaNO_3$ and MAFM-350-2-KNO_3 with the displayed concentric circles. Figure 4.3 shows the HRTEM and SAED images of the commercial IrO_2. Concentric circles can also be seen for the commercial IrO_2, confirming the particles are not polycrystalline. In Table 4.2, MAFM-350-2-$NaNO_3$ had the smallest particle sizes. It can be assumed that smaller particle

sizes may have higher geometric surface areas and promotes the electrochemical activities of the metal oxide [115, 116].

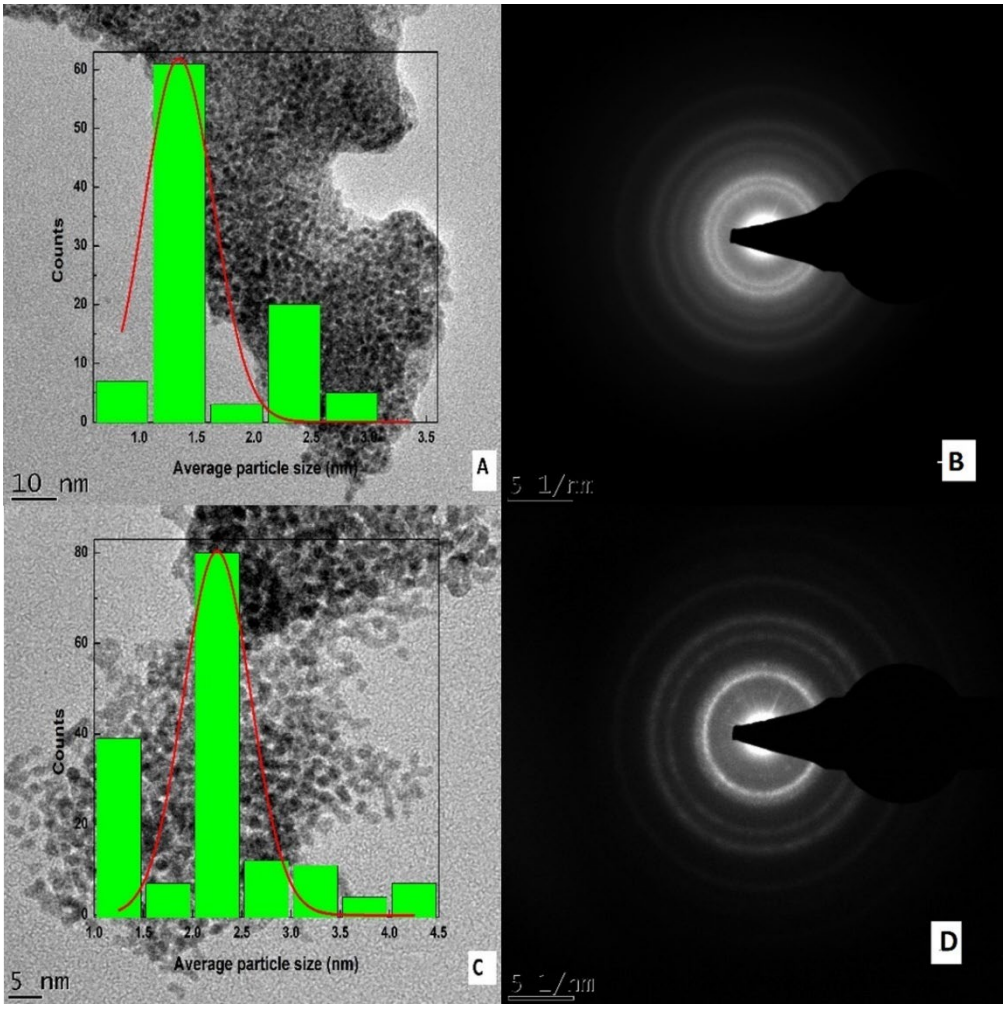

Figure 4.2: HRTEM and SAED analysis of (A) and (B) MAFM-350-2-$NaNO_3$, and (C) and (D) MAFM-350-2-KNO_3.

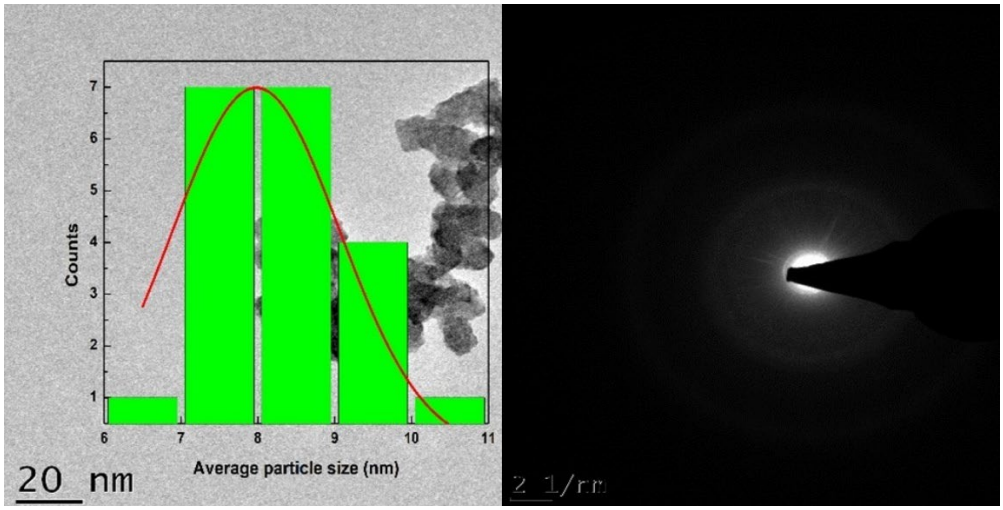

Figure 4.3: HRTEM and SAED analysis of the commercial IrO_2.

Table 4.2: Average HRTEM particle sizes of commercial IrO_2 and IrO_2 synthesized using the MAFM with $NaNO_3$ and KNO_3.

Sample name	Average particle size (nm)
MAFM-350-2-$NaNO_3$	2.31
MAFM-350-2-KNO_3	2.08
Commercial IrO_2	8.69

The specific surface area of the commercial IrO_2 and the IrO_2 synthesized with the MAFM when using $NaNO_3$ and KNO_3 were measured with the BET analysis. The specific surface area is given as the average diameter of the particles by determining the particle-size-dependent area and the charge-deduced area [24]. The use of different reagents not only affects the particle shape, but also the dispersion of the metal oxide [77]. The N_2 adsorption-desorption results of the IrO_2 are summarized in Table 4.3. MAFM-350-2-$NaNO_3$ has the highest BET surface area of 216.23 m^2/g. The change in reagent resulted in a change in the BET surface area. The commercial IrO_2 had the smallest BET surface area which may be due to the larger particle sizes [75].

Table 4.3: BET surface area of the commercial IrO_2 and IrO_2 synthesized using the MAFM with $NaNO_3$ and KNO_3.

Sample name	BET surface area (m^2/g)
MAFM-350-2-$NaNO_3$	216.23
MAFM-350-2-KNO_3	167.52
Commercial IrO_2	25.11

The cyclic voltammograms were obtained between a potential window of 0 and +1.4 V vs. RHE with a potential scan rate of 20 mVs^{-1}. The cyclic voltammograms seem to be influenced by the reagents used since there is a change in the two redox couples, Ir(III)/Ir(IV) and Ir(IV)/Ir(V) (Table 4.4). Figure 4.4 shows the Ir(III)/Ir(IV) and Ir(IV)/Ir(V) anodic oxidation peaks for MAFM-350-2-$NaNO_3$, MAFM-350-2-KNO_3 and commercial IrO_2. Both the maximum current density of the commercial IrO_2 were lower when compared to MAFM-350-2-$NaNO_3$ and MAFM-350-2-KNO_3. For both the forward (anodic) and reverse (cathodic) scans, an additional peak was seen at +0.35 V vs. RHE for MAFM-350-2-$NaNO_3$. The additional peak can also be seen for the commercial IrO_2. The cause of the peaks may be due to a coupled ion-electron transfer, formal potential distribution, relations in the layer, or the change in mass transport within the layer as the potential change [117]. Similar cyclic voltammograms as that of the MAFM-350-2-$NaNO_3$ were obtained by Liu et al. [74].

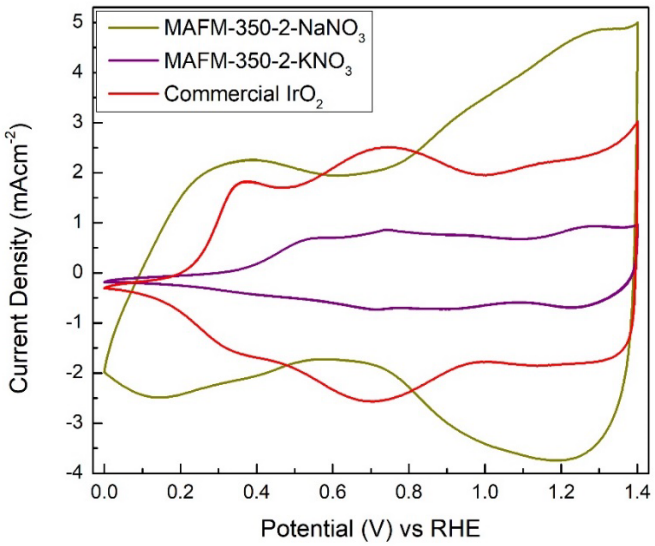

Figure 4.4: CV analysis in 0.5 M H_2SO_4.of the commercial IrO_2 and IrO_2 synthesized using the MAFM with $NaNO_3$ and KNO_3.

Table 4.4: Anodic peak potentials of the Ir(III)/Ir(IV) and Ir(IV)/Ir(V) redox couples of the commercial IrO_2 and IrO_2 synthesized using the MAFM with $NaNO_3$ and KNO_3.

Sample name	Ir(III)/Ir(IV) redox couple (V vs. RHE)	Ir(IV)/Ir(V) redox couple (V vs. RHE)
MAFM-350-2-$NaNO_3$	+0.94	+1.30
MAFM-350-2-KNO_3	+0.74	+1.26
Commercial IrO_2	+0.74	+1.16

The polarization curves were obtained using the LSV technique which was performed between +1.0 and +1.8 V vs. RHE at a potential scan rate of 2 mVs^{-1}. Table 4.5 summarizes the OER overpotential, electrode potential at different current densities, and the Tafel slopes of the IrO_2. The polarization curves of the commercial IrO_2 and IrO_2 synthesized with the MAFM using $NaNO_3$ vs. KNO_3, are shown in Figure 4.5. The MAFM-350-2-$NaNO_3$ has the lowest overpotential, at 10 $mAcm^{-2}$, when compared to the MAFM-350-2-KNO_3. The onset potentials of the synthesized IrO_2 were found to be at ~1.5 V vs. RHE due to the energy requirement during the H_2O phase transition. At lower current densities (<150 $mAcm^{-2}$), the MAFM-350-2-$NaNO_3$ had higher OER

activities. The commercial IrO_2 had a higher OER activity at increased current densities (>150 $mAcm^{-2}$). The reason for including the current density at 150 $mAcm^{-2}$ because it is the highest available current density that all three IrO_2 can maintain before the formation of O_2 gas on the electrode which results in a cut-off potential. Falcao et al. [44] shows how produced gas bubbles can block the active surface area of catalysts during high current densities. The lower OER activities of MAFM-350-2-KNO_3 and commercial IrO_2 can be attributed to the larger particle sizes as shown by the HRTEM analysis and the smaller BET surface areas. The corresponding Tafel slopes of the IrO_2 are estimated to be about 40 mV dec^{-1} which is consistent with most anodically produced IrO_2 electrodes [118]. When comparing the Tafel slopes, the commercial IrO_2 had the smallest slope. IrO_2 with a smaller Tafel slope generates current more efficiently when voltage is applied [75, 121].

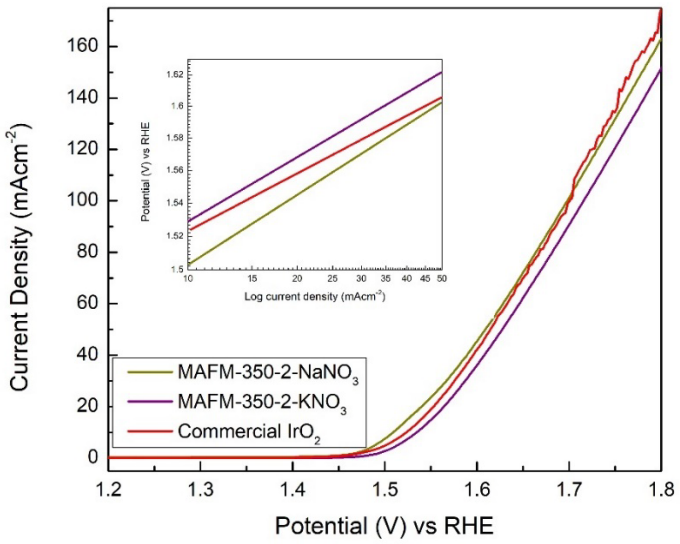

Figure 4.5: LSV analysis in 0.5M H_2SO_4 of the commercial IrO_2 and IrO_2 synthesized using the MAFM with $NaNO_3$ and KNO_3.

Table 4.5: Overpotential, onset potential, and the Tafel slopes of the commercial IrO_2 and IrO_2 synthesized using the MAFM with $NaNO_3$ and KNO_3.

Sample name	Overpotential at 10 $mAcm^{-2}$ (V vs. RHE)	Electrode potential at 50 $mAcm^{-2}$ (V vs. RHE)	Electrode potential at 150 $mAcm^{-2}$ (V vs. RHE)	Tafel slopes 10-50 $mAcm^{-2}$ ($mV\ dec^{-1}$)
MAFM-350-2-$NaNO_3$	0.28	1.61	1.79	40.54
MAFM-350-2-KNO_3	0.31	1.63	1.80	40.59
Commercial IrO_2	0.29	1.62	1.77	40.32

CP analysis was performed at 10 $mAcm^{-2}$ until the potential reached a potential of 1.8 V vs. RHE. Performance degradation is normally attributed to dissolution of the IrO_2 catalyst [12, 118]. Figure 4.6 shows the CP analysis of the IrO_2 synthesized with the MAFM using $NaNO_3$ and KNO_3 as well as the commercial IrO_2 catalyst. MAFM-350-2-$NaNO_3$ had the highest OER stability (~82 hrs) before reaching the cut-off potential. The OER stability of the commercial IrO_2 and synthesized IrO_2 catalysts are summarized in Table 4.6. Lim et al. [79] also observed improved OER performance for IrO_2 when $NaNO_3$ was used during the synthesis. The larger BET surface area may explain the significantly improved OER stability of MAFM-350-2-$NaNO_3$. The XRD analysis also showed a better developed crystallinity structure for MAFM-350-2-$NaNO_3$ when compared to MAFM-350-2-KNO_3. When using KNO_3, synthesis temperatures above its melting point should be considered which may have affected the crystallization and crystallite sizes.

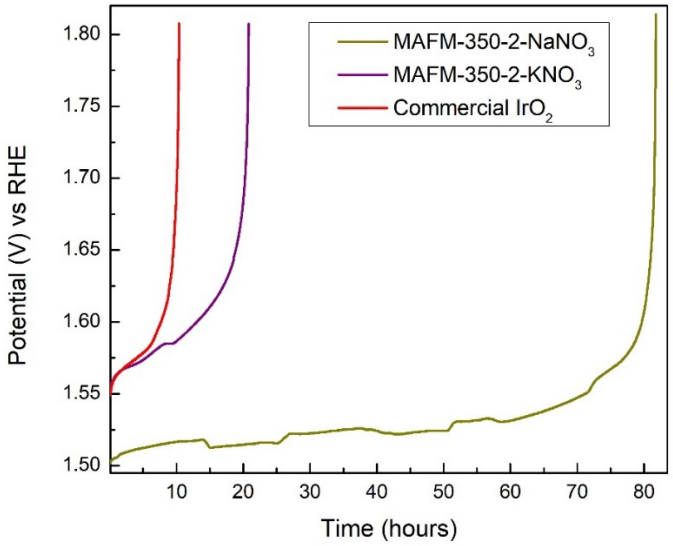

Figure 4.6: CP analysis in 0.5 M H_2SO_4 of the commercial IrO_2 and IrO_2 synthesized using the MAFM with $NaNO_3$ and KNO_3.

Table 4.6: OER stability of the commercial IrO_2 and IrO_2 synthesized using the MAFM with $NaNO_3$ and KNO_3.

Sample name	Stability (hrs)
MAFM-350-2-$NaNO_3$	81.8
MAFM-350-2-KNO_3	20.82
Commercial IrO_2	10.4

4.1.2 Effect of temperature on the IrO_2 catalysts

To investigate the effect of synthesis temperatures, the synthesis duration and reagents used remained constant. The previous section confirmed the improved IrO_2 performances when using the $NaNO_3$ reagent. A 2 hrs synthesis duration was most efficient to synthesize IrO_2, as confirmed by Felix et al. [119]. Figure 4.6 shows the XRD spectra for the IrO_2 catalysts synthesized at temperatures 350, 500, and 650℃ as well as the commercial IrO_2 catalyst. The peaks were assigned using the JCP2 standard files for IrO_2 (JCP2_150870) and Ir (JCP2_06–0598). In Figure 4.7, the sharpening of the peaks with increased synthesis temperatures show the phase transition from an

amorphous to a highly crystalline IrO_2. The increased crystallinity was seen by the sharpening of the diffraction peaks, which are also known to produce larger crystallite sizes. This observation is common for the MAFM since $NaNO_3$ is used as the oxidizing agent [70]. However, the MAFM-350-2-$NaNO_3$ was in the amorphous phase which is characterized by broad diffraction peaks [114]. The (110) and (101) facets are important stable facets for IrO_2 and were seen in samples MAFM-500-2-$NaNO_3$ and MAFM-650-2-$NaNO_3$, while only facet (101) was present in MAFM-350-2-$NaNO_3$. Furthermore, the (211) facet at *Bragg* angle ~54° was present in both MAFM-500-2-$NaNO_3$ and MAFM-650-2-$NaNO_3$ due to the increased crystallization at higher temperatures. A similar observation of increased crystallinity with increased synthesis temperatures, i.e. 500 and 650℃, was seen by Arico et al. [35]. At the *Bragg* angle of ~40°, metallic Ir was seen in MAFM-500-2-$NaNO_3$, MAFM-650-2-$NaNO_3$, and commercial IrO_2. The average IrO_2 crystallite sizes were determined, using the Scherrer formula at (101) facet, and summarized in Table 4.7. The MAFM-350-2-NaNO3 had the smallest crystallite sizes and as expected, MAFM-650-2-NaNO3 had the largest crystallite sizes.

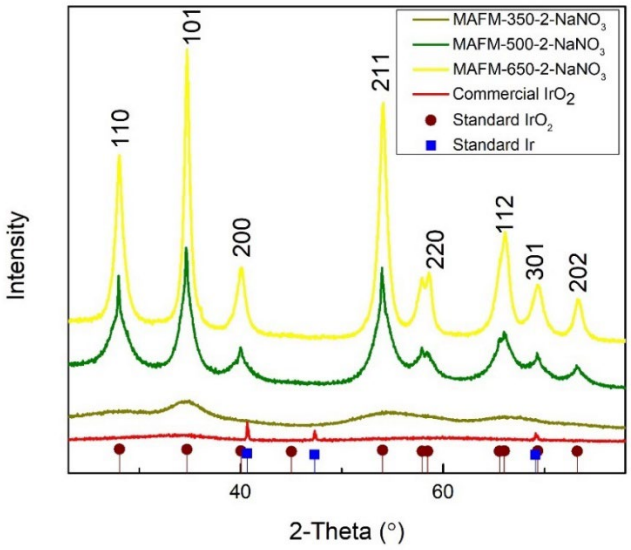

Figure 4.7: XRD analysis of the commercial IrO_2 and IrO_2 synthesized using the MAFM at temperatures 350, 500, and 650℃.

Table 4.7: Average crystallite sizes calculated using the Scherrer equation of the commercial IrO_2 and the IrO_2 synthesized using the MAFM at temperatures 350, 500, and 650℃.

Sample Name	IrO_2 Crystallite Size (nm) by Scherrer Formula
MAFM-350-2-$NaNO_3$	2.73
MAFM-500-2-$NaNO_3$	7.78
MAFM-650-2-$NaNO_3$	10.01
Commercial IrO_2	0

The morphology of the synthesized IrO_2 catalysts were studied using HRTEM analysis. As previously mentioned, MAFM-350-2-$NaNO_3$ had uniform spherical particles with small crystalline regions. MAFM-500-2-$NaNO_3$ (Figure 4.8C) had cubic-shaped particles whereas MAFM-650-2-$NaNO_3$ (Figure 4.8E) had a combination of cubic and cylindrical-shaped particles. The width and length of the cylindrical shaped particles of MAFM-650-2-$NaNO_3$ are 5 and 11 nm respectively. The sharp rings in Figure 4.7D and Figure 4.8F confirmed the highly crystalline nature of the IrO_2. Subramanian et al. [35] showed similar SAED patterns for IrO_2 synthesized at increased temperatures. The specific surface energy of growing crystal facets may explain the variation in particle shapes of the synthesized IrO_2 [77]. Table 4.8 summarizes the average particle sizes of the synthesized IrO_2 and commercial IrO_2.

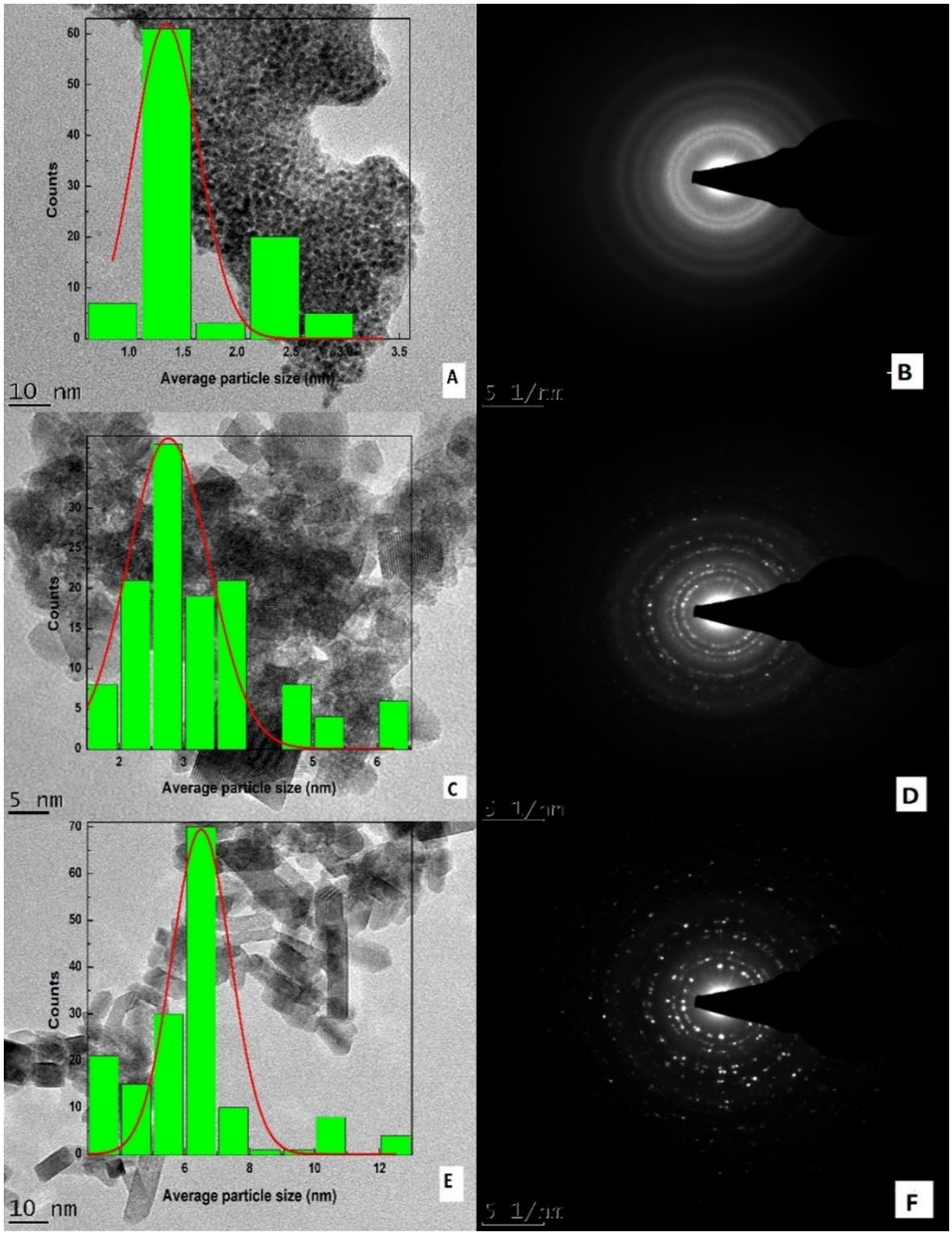

Figure 4.8: HRTEM and SAED analysis of (A) and (B) MAFM-350-2-$NaNO_3$, (C) and (D) MAFM-500-2-$NaNO_3$, and (E) and (F) MAFM-650-2-$NaNO_3$.

Table 4.8: Average HRTEM particle sizes of commercial IrO_2 and IrO_2 synthesized using the MAFM at temperatures 350, 500, and 650℃.

Sample name	Average particle size (nm)
MAFM-350-2-$NaNO_3$	2.31
MAFM-500-2-$NaNO_3$	3.54
MAFM-650-2-$NaNO_3$	Width: 5.23 Length: 11.36
Commercial IrO_2	8.69

The BET analysis measured the specific surface area of the IrO_2 synthesized at temperatures 350, 500, and 650℃ using the MAFM. Table 4.9 summarizes the N_2 adsorption-desorption results of the IrO_2 catalysts. As the synthesis temperatures decreased, the BET surface area of the synthesized IrO_2 increased. MAFM-350-2-$NaNO_3$ has the largest BET surface area of 216.23 m^2/g. The larger BET surface area is an indication of the smaller IrO_2 particles, confirming the HRTEM analysis results. However, the commercial IrO_2 had the smallest BET surface area when compared to the synthesized IrO_2 which could be due to the presence of metallic Ir as seen in the XRD analysis.

Table 4.9: BET surface areas of the commercial IrO_2 and IrO_2 synthesized using the MAFM at temperatures 350, 500, and 650℃.

Sample name	BET surface area (m^2/g)
MAFM-350-2-$NaNO_3$	216.23
MAFM-500-2-$NaNO_3$	104.84
MAFM-650-2-$NaNO_3$	53.84
Commercial IrO_2	25.11

The CV analysis was obtained at a potential scan rate of 20 mVs^{-1} in a potential window of 0 and +1.4 V vs. RHE. The slight shift in the two redox couples, Ir(III)/Ir(IV) and Ir(IV)/Ir(V), show that the cyclic voltammograms seem to be influenced by the synthesis temperatures (Table 4.10). Figure 4.9 shows the Ir(III)/Ir(IV) and Ir(IV)/Ir(V) anodic

oxidation peaks of MAFM-350-2-$NaNO_3$, MAFM-500-2-$NaNO_3$, MAFM-650-2-$NaNO_3$, and the commercial IrO_2. Between 0 and +0.65 V vs. RHE, no charges were transferred for the MAFM-500-2-$NaNO_3$ and MAFM-650-2-$NaNO_3$ due to the double layer charging [68]. IrO_2 synthesized at 500 and 650℃ does not show the additional peak, as seen by MAFM-350-2-$NaNO_3$ at +0.35 V vs. RHE, which rules out that it may be due to the oxidation/reduction sodium layer impurity. Upon the cathodic potential scan at 0 V vs. RHE, a strong negative "tail" was seen for MAFM-500-2-$NaNO_3$ and MAFM-650-2-$NaNO_3$. This reflects their negative capacitive behaviour (H_{ads}), involving the double layer- and pseudo capacitances [68, 120]. The CV curves have similar shapes to those found by Rasten et al. [72].

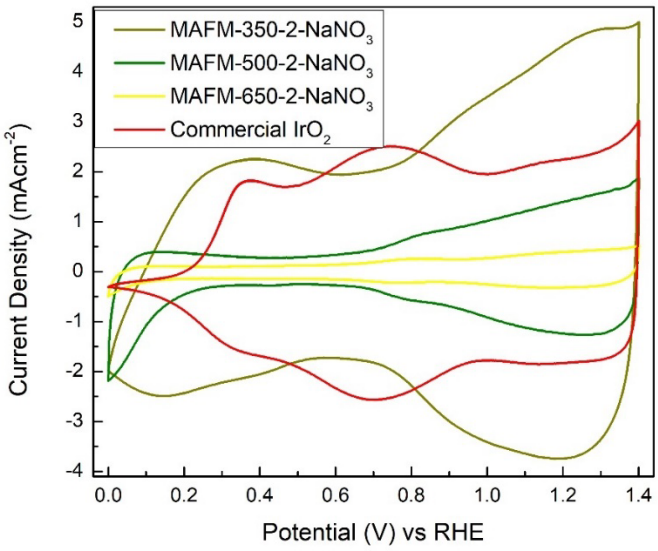

Figure 4.9: CV analysis in 0.5 M H_2SO_4 of the commercial IrO_2 and IrO_2 synthesized using the MAFM at temperatures 350, 500, and 650℃.

Table 4.10: Anodic peak potentials of the Ir(III)/Ir(IV) and Ir(IV)/Ir(V) redox couples of the commercial IrO_2 and IrO_2 synthesized using the MAFM at temperatures 350, 500, and 650℃.

Sample name	Ir(III)/Ir(IV) redox couple (V vs. RHE)	Ir(IV)/Ir(V) redox couple (V vs. RHE)
MAFM-350-2-$NaNO_3$	+0.94	+1.30
MAFM-500-2-$NaNO_3$	+0.82	+1.28
MAFM-650-2-$NaNO_3$	+0.78	+1.18
Commercial IrO_2	+0.74	+1.16

Figure 4.10 shows the polarization curves produced by the LSV technique at a potential scan rate of 2 mVs^{-1} between +1.2 and +1.8 V vs. RHE. Table 4.11 summarizes the OER overpotential, the electrode potential at different current densities, and the Tafel slopes of the IrO_2. The MAFM-350-2-$NaNO_3$ has the lowest overpotential at 10 $mAcm^{-2}$ when compared to the IrO_2 synthesized at 500 and 650℃. At lower current densities (<25 $mAcm^{-2}$), the MAFM-350-2-$NaNO_3$ had higher OER activities. However, at increased current densities (> 25 $mAcm^{-2}$) the MAFM-500-2-$NaNO_3$ had higher OER activities. No results were produced at 150 $mAcm^{-2}$ for MAFM-650-2-$NaNO_3$ due to the IrO_2 degradation caused by the Ir dissolution [118]. When comparing the Tafel slopes, MAFM-500-2-$NaNO_3$ had the lowest Tafel slope value and produces current density more efficiently when a voltage is applied [75, 121]. The lower OER activities of MAFM-650-2-$NaNO_3$ and commercial IrO_2 can be attributed to the larger particle sizes as shown by the HRTEM analysis. Felix et al. [68] also observed higher OER activities for the IrO_2 synthesized at lower synthesis temperatures.

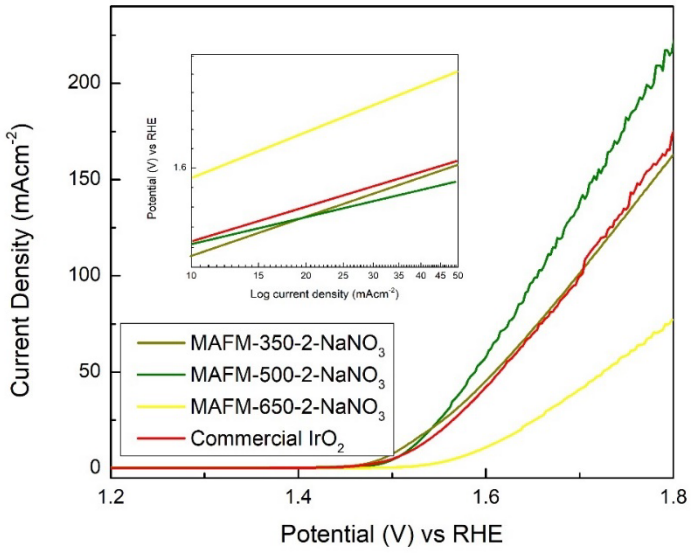

Figure 4.10: LSV analysis in 0.5 M H_2SO_4 of the commercial IrO_2 and IrO_2 synthesized using the MAFM at temperatures 350, 500, and 650℃.

Table 4.11: Overpotential, electrode potentials, and the Tafel slopes of the commercial IrO_2 and IrO_2 synthesized using the MAFM at temperatures 350, 500, and 650℃.

Sample name	Overpotential at 10 mAcm^{-2} (V vs. RHE)	Onset potential at 50 mAcm^{-2} (V vs. RHE)	Onset potential at 150 mAcm^{-2} (V vs. RHE)	Tafel slopes 10-50 mAcm^{-2} (mV dec^{-1})
MAFM-350-2-NaNO$_3$	0.28	1.61	1.79	40.54
MAFM-500-2-NaNO$_3$	0.29	1.59	1.72	40.24
MAFM-650-2-NaNO$_3$	0.36	1.73	-	40.42
Commercial IrO$_2$	0.29	1.62	1.77	40.32

CP analysis was performed at 10 mAcm^{-2} until the potential reached a potential of 1.8 V vs. RHE. Figure 4.11 shows the performance of the IrO_2 catalysts synthesized with the MAFM at temperatures 350, 500, and 650℃. MAFM-350-2-$NaNO_3$ had the highest OER stability of ~82 hrs while MAFM-650-2-$NaNO_3$ had the lowest OER stability. The OER stability of the IrO_2 catalysts was summarized in Table 4.12. Felix et al. [68] also showed improved OER stability of IrO_2 synthesized at a lower temperature, i.e.,

350℃. The highly crystalline nature of MAFM-650-2-$NaNO_3$ may have caused a decrease in the OER stability, resulting in the sample being out-performed by the commercial IrO_2.

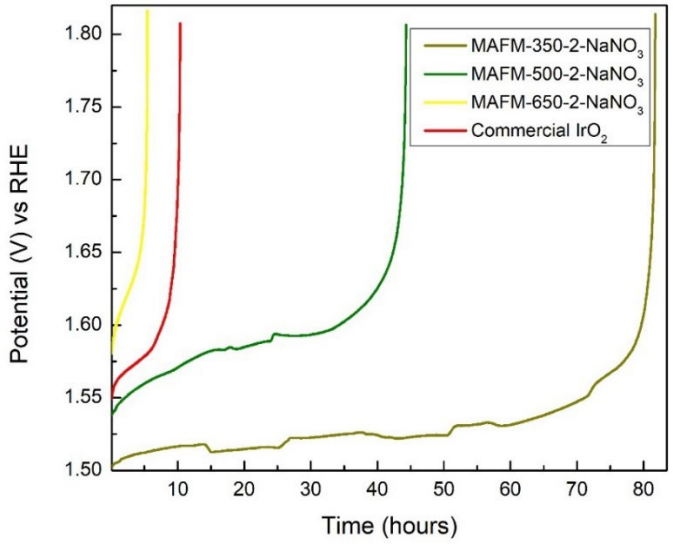

Figure 4.11: CP analysis in 0.5M H_2SO_4 of the commercial IrO_2 and IrO_2 synthesized using the MAFM at temperatures 350, 500, and 650℃.

Table 4.12: OER stability of the commercial IrO_2 and IrO_2 synthesized using the MAFM at temperatures 350, 500, and 650℃.

Sample name	Stability (hrs)
MAFM-350-2-$NaNO_3$	81.8
MAFM-500-2-$NaNO_3$	44.3
MAFM-650-2-$NaNO_3$	5.5
Commercial IrO_2	10.4

4.2 Molten Salt method

4.2.1 Effect of reaction duration on the IrO_2 catalysts

To study the effect of synthesis duration (4 and 8 hrs), the synthesis temperature (650℃) and reagent (NaCl) used remained constant for the MSM. A synthesis temperature of

650℃ was proven to be suitable for the MSM by Ahmed et al. [66]. No significant difference was seen in the IrO_2 yield between the reagents NaCl/KCl and NaCl [77]. Therefore, only the NaCl reagent was used for the MSM experiments. The XRD spectra of the commercial IrO_2 and IrO_2 synthesized with the MSM are shown in Figure 4.12. The JCP2 standard files for IrO_2 (JCP2_150870) and Ir (JCP2_06–0598) were used to assign the sample peaks. From the XRD spectra, both MSM-650-4-NaCl and MSM-650-8-NaCl have sharp diffraction peaks which indicates their large crystallinity sizes. The increased synthesis temperature and duration may have contributed to the increased crystallinity [68, 114]. This allowed the formation of facet (211) at *Bragg* angle ~54° for the synthesized IrO_2. The important stable facets (110) and (101) were also seen in both MSM-650-4-NaCl and MSM-650-8-NaCl. At *Bragg* angle of ~40° and ~69°, an overlap of IrO_2 and Ir was shown for both MSM-650-4-NaCl and MSM-650-8-NaCl. However, at *Bragg* angle ~47° only metallic Ir was present for MSM-650-4-NaCl and the commercial IrO_2. Table 4.13 summarizes the IrO_2 crystallite sizes, at the (101) facet, which was calculated using the Scherrer formula (Equation 23). A direct correlation was seen between the average crystallite size and synthesis duration, as demonstrated by Zhou et al. [77]. However, the presence of metallic Ir in MSM-650-4-NaCl and the commercial IrO_2 may have contributed to the decreased OER performance [17, 119].

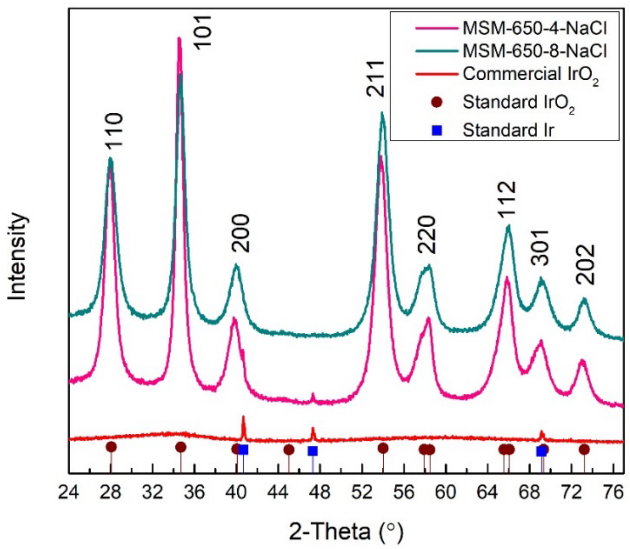

Figure 4.12: XRD patterns of the commercial IrO_2 and IrO_2 synthesized using the MSM at durations 4 and 8 hrs.

Table 4.13: Average crystallite sizes calculated using the Scherrer equation of the commercial IrO_2 and the IrO_2 synthesized using the MSM at duration 4 and 8 hrs.

Sample name	IrO_2 Crystallite Size (nm) by Scherrer Formula
MSM-650-4-NaCl	12.43
MSM-650-8-NaCl	8.78
Commercial IrO_2	0

The morphology of the IrO_2 synthesized with the MSM at durations 4 and 8 hrs were studied using the HRTEM analysis. Both MSM-4-650-NaCl and MSM-8-650-NaCl consisted of various particle shapes (spherical, cubic, and cylindrical) with various sizes (Figure 4.13A and Figure 4.13C). Most of the MSM-4-650-NaCl particles were cylindrical shaped while the bulk of the particles for MSM-8-650-NaCl was cubic shaped. Zhou et al. [77] observed similar changes in morphology with the change in the synthesis duration. The SAED images, Figure 4.13B and Figure 4.13D, confirmed the larger crystalline regions of MSM-4-650-NaCl and MSM-8-650-NaCl, which were seen by the XRD analysis. Table 4.14 summarizes the average particle sizes with MSM-650-8-NaCl having slightly smaller particle sizes than MSM-650-4-NaCl.

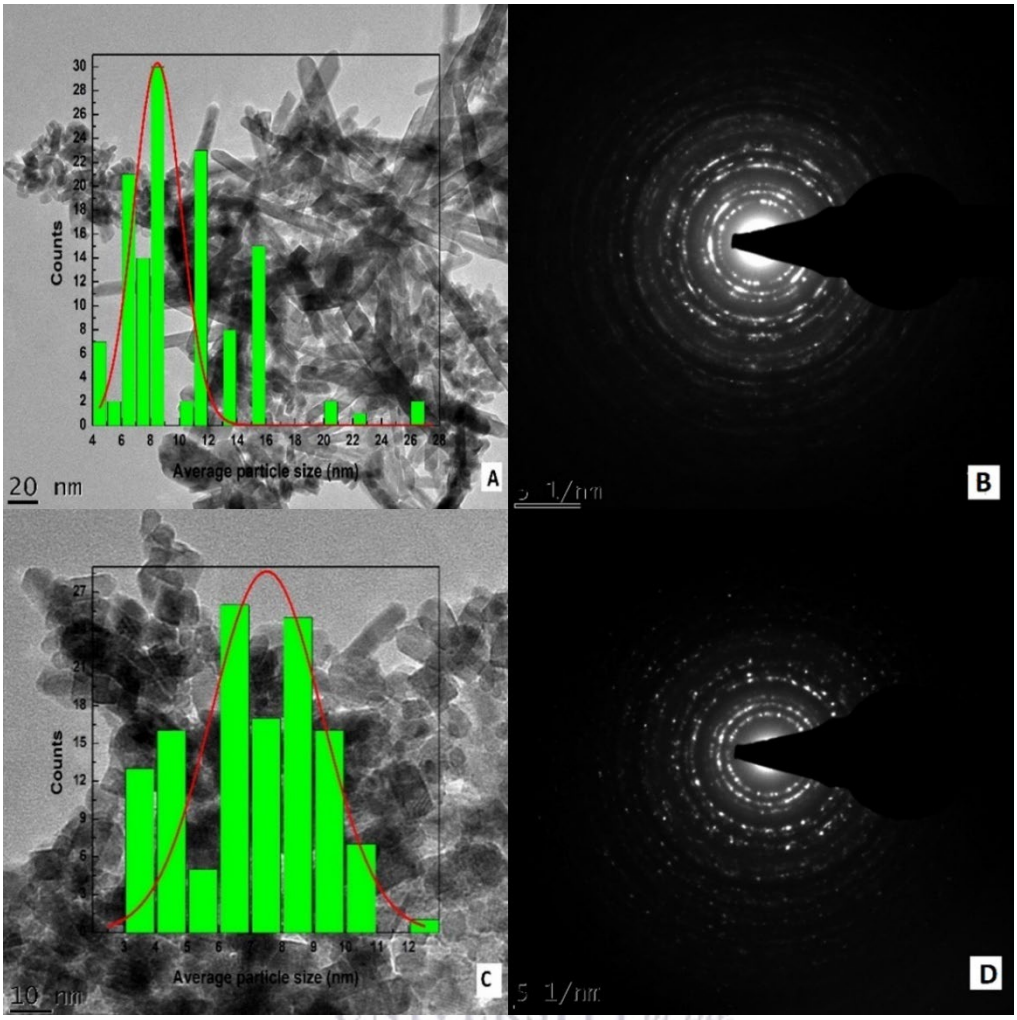

Figure 4.13: HRTEM and SAED analysis of (A) and (B) MSM-650-4-NaCl, and (C) and (D) MSM-650-8-NaCl.

Table 4.14: Average HRTEM particle sizes of commercial IrO_2 and IrO_2 synthesized using the MSM at durations 4 and 8hrs.

Sample name	Average particle size (nm)
MSM-650-4-NaCl	Width: 2.73 Length: 26.36
MSM-650-8-NaCl	8.18
Commercial IrO_2	8.69

The BET analysis was used to study the specific surface area of the commercial IrO_2 and IrO_2 synthesized using the MSM at synthesis durations 4 and 8 hrs. Table 4.15 summarizes the N_2 adsorption-desorption results of the IrO_2 samples. The BET surface

area of the synthesized IrO_2 increased with increasing synthesis duration. The MSM-650-8-NaCl has the highest BET surface area of 54.69 m^2/g. This confirms the smaller IrO_2 particle sizes seen in the HRTEM analysis. The presence of metallic Ir in MSM-650-4-NaCl, as seen from the XRD analysis, may be responsible for the decreased active surface area [124]. Furthermore, the commercial IrO_2 had the smallest BET surface area when compared to the synthesized IrO_2.

Table 4.15: BET surface areas of the commercial IrO_2 and IrO_2 synthesized using the MSM at durations 4 and 8 hrs.

Sample name	BET surface area (m^2/g)
MSM-650-4-NaCl	31.77
MSM-650-8-NaCl	54.69
Commercial IrO_2	25.11

The CV analysis was performed between a potential of 0 and +1.4 V vs. RHE with a potential scan rate of 20 mVs^{-1}. There is a slight shift in the two redox couples, Ir(III)/Ir(IV) and Ir(IV)/Ir(V), confirming that the synthesis conditions have influenced the properties of the synthesized IrO_2. The Ir(III)/Ir(IV) and Ir(IV)/Ir(V) anodic oxidation peaks for MSM-650-4-NaCl, MSM-650-8-NaCl, and the commercial IrO_2 are shown in Figure 4.14 and summarized in Table 4.16. Negative capacitive behaviour (H_{ads}) can be seen for both MSM-650-4-NaCl and MSM-650-8-NaCl. This negative capacitive behaviour can also be seen by Felix et al. [68, 120]. Furthermore, both the MSM-650-4-NaCl and MSM-650-8-NaCl were not fully reduced during the cathodic scan and some IrO_2 species did not oxidize during the anodic scan. The small oxidizing peak, at 0 V vs. RHE, for MSM-650-4-NaCl shows the presence of hydrogen adsorption on the negative (cathodic) scan and hydrogen evolution on the positive (cathodic) scan.

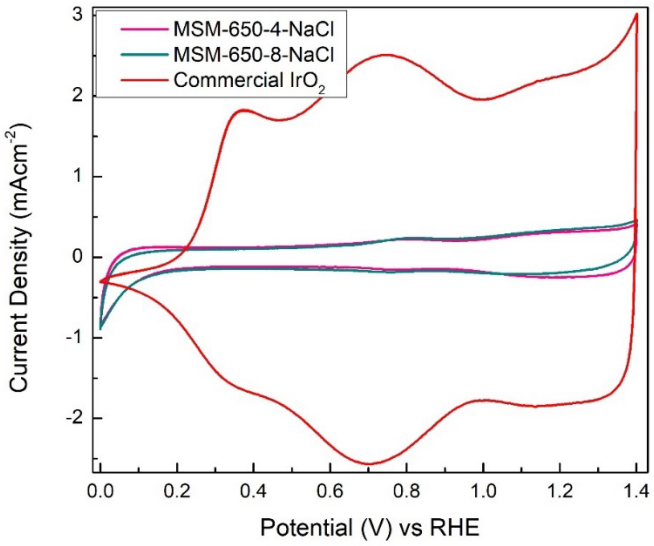

Figure 4.14: CV analysis in 0.5 M H_2SO_4 of the commercial IrO_2 and IrO_2 synthesized using the MSM at durations 4 and 8 hrs.

Table 4.16: Anodic peak potentials of the Ir(III)/Ir(IV) and Ir(IV)/Ir(V) redox couples of the commercial IrO_2 and IrO_2 synthesized using the MSM at durations 4 and 8 hrs.

Sample name	Ir(III)/Ir(IV) redox couple (V vs. RHE)	Ir(IV)/Ir(V) redox couple (V vs. RHE)
MSM-650-4-NaCl	+0.78	+1.17
MSM-650-8-NaCl	+0.79	+1.19
Commercial IrO_2	+0.74	+1.16

The LSV analysis produced polarization curves at a potential scan rate of 2 mVs^{-1} between +1.2 and +1.8 V vs. RHE (Figure 4.14). OER overpotential, electrode potential at different current densities, and the Tafel slopes of the commercial IrO_2 and synthesized IrO_2 are summarized in Table 4.15. At 10 $mAcm^{-2}$, MSM-650-4-NaCl has the lowest overpotential, which corresponds to a higher OER activity. MSM-650-4-NaCl also has higher electrode potentials at increased current densities (>40 $mAcm^{-2}$). When comparing the Tafel slopes, MSM-650-4-NaCl had the smallest slope value. Tafel slopes with smaller values usually produce current more efficiently with applied voltage [78, 121].

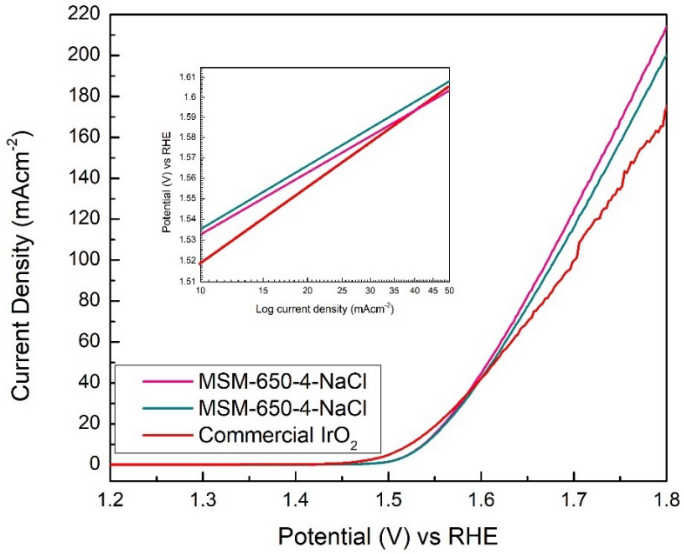

Figure 4.15: LSV analysis in 0.5M H_2SO_4 of the commercial IrO_2 and IrO_2 synthesized using the MSM at durations 4 and 8 hrs.

Table 4.17: Overpotential, onset potentials, and the Tafel slopes of the commercial IrO_2 and IrO_2 synthesized using the MSM at durations 4 and 8 hrs.

Sample name	Overpotential at 10 $mAcm^{-2}$ (V vs. RHE)	Onset potential at 50 $mAcm^{-2}$ (V vs. RHE)	Onset potential at 150 $mAcm^{-2}$ (V vs. RHE)	Tafel slopes 10-50 $mAcm^{-2}$ ($mV\ dec^{-1}$)
MSM-650-4-NaCl	0.31	1.61	1.73	40.46
MSM-650-8-NaCl	0.32	1.62	1.74	40.48
Commercial IrO_2	0.29	1.62	1.77	40.32

The CP analysis was performed at 10 $mAcm^{-2}$ until it reached a cut-off potential of 1.8 V vs. RHE (Figure 4.16). Table 4.18 summarizes the OER stability of the IrO_2 synthesized with the MSM at durations 4 and 8 hrs. MSM-4-650-NaCl had the highest stability of ~41 hrs, whereas the measured stability of MSM-8-650-NaCl was only ~20 hrs. Therefore, the OER stability of the IrO_2 is strongly dependent on the synthesis duration [124]. MSM-650-4-NaCl experienced a significant amount of O_2 bubble adsorption onto the IrO_2 surface at the start of the experiment, which is known to decrease the ohmic measurements [119].

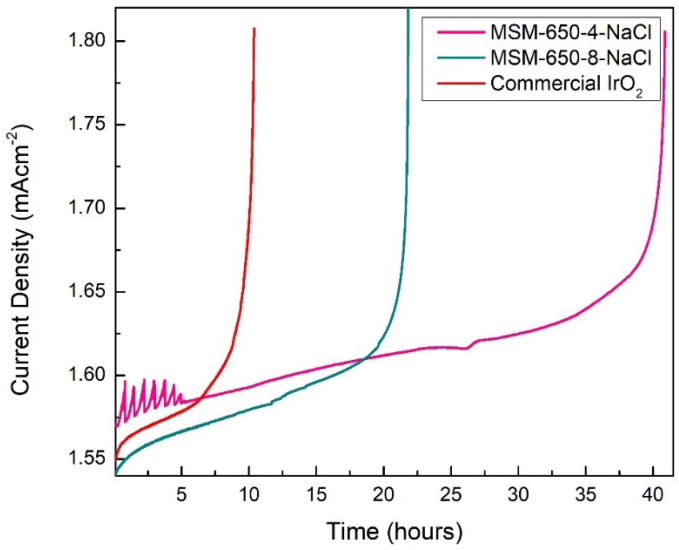

Figure 4.16: CP analysis in 0.5 M H_2SO_4 of the commercial IrO_2 and IrO_2 synthesized using the MSM at durations 4 and 8hrs.

Table 4.18: OER stability of the commercial IrO_2 and IrO_2 synthesized using the MSM at durations 4 and 8 hrs.

Sample name	Stability (hrs)
MSM-650-4-NaCl	40.9
MSM-650-8-NaCl	22.4
Commercial IrO_2	10.4

4.2.2 Effect of synthesis temperature on the IrO_2 catalysts

To study the effect of the MSM synthesis temperatures, the synthesis duration and reagent remained constant. In section 4.2.1, a synthesis duration of 4 hrs and the use of NaCl reagent were proven to synthesize IrO_2 with improved performances. Figure 4.17 shows the XRD spectra of the IrO_2 synthesized using the MSM at temperatures 350, 500, and 650℃. The JCP2 standard files for IrO_2 (JCP2_150870) and Ir (JCP2_06–0598) were used to assign the peaks. The sharpening of the diffraction peaks with increased synthesis temperatures indicates the phase transition from amorphous to the crystalline phase between the IrO_2. Lower crystallite sizes are associated with IrO_2 in the amorphous phase, which can be seen by the broad peaks of MSM-350-4-NaCl.

Larger crystallite sizes are associated with IrO_2 in the crystalline phase, as seen in MSM-500-4-NaCl and MSM-650-4-NaCl. The sharpening of the diffraction peaks with increasing synthesis temperatures can also be seen by Liu et al. [74]. Important stable facets (110) and (211) were only present in MSM-500-4-NaCl and MSM-650-4-NaCl, while only (101) facet was seen in MSM-350-4-NaCl. At the *Bragg's* angle of ~45°, the metallic Ir was only present in MSM-650-4-NaCl. At facet (101), the Scherrer formula, Equation 23, was used to determine the IrO_2 crystallite sizes and summarized in Table 4.19. The MSM-350-4-NaCl had the smallest crystallite sizes, while MSM-650-4-NaCl had the largest crystallite size.

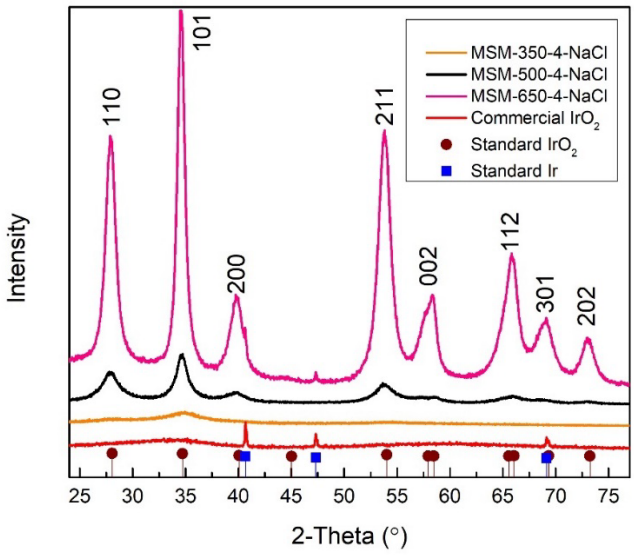

Figure 4.17: XRD analysis of the commercial IrO_2 and IrO_2 synthesized using the MSM at temperatures 350, 500, and 650℃.

Table 4.19: Average crystallite sizes calculated using the Scherrer equation of the commercial IrO_2 and the IrO_2 synthesized using the MSM at temperatures 350, 500, and 650℃.

Sample name	IrO_2 Crystallite Size (nm) by Scherrer formula
MSM-350-4-NaCl	2.83
MSM-500-4-NaCl	7.05
MSM-650-4-NaCl	12.43
Commercial IrO_2	0

HRTEM analysis was used to study the morphology of the IrO_2 catalysts. The MSM is known to produce IrO_2 with different particle shapes and sizes [66, 77]. The MSM-350-4-NaCl had undefined particles with sizes of about 4.12 nm (Figure 4.18A). Concentric circles were displayed in the SAED image in Figure 4.18B for MSM-350-4-NaCl, confirming the smaller crystalline region found in the XRD analysis. Figure 4.18C showed a combination of cubic and cylindrical particles for MSM-500-4-NaCl. The MSM-650-4-NaCl consisted of various particle shapes (spherical, cubic, and cylindrical), each with various particle sizes (Figure 4.18E). The width and length of the cylindrical particles are 9 and 61 nm respectively. IrO_2 synthesized at increased temperatures (500 and 650℃) showed increased crystallinity sizes which are confirmed in Figure 4.18D and Figure 4.18F by the defined concentric circles. Ahmed et al [66] also produced IrO_2 with decreased particle sizes at lower synthesis temperatures. Table 4.20 summarizes the particle sizes of the commercial IrO_2 and IrO_2 synthesized with the MSM.

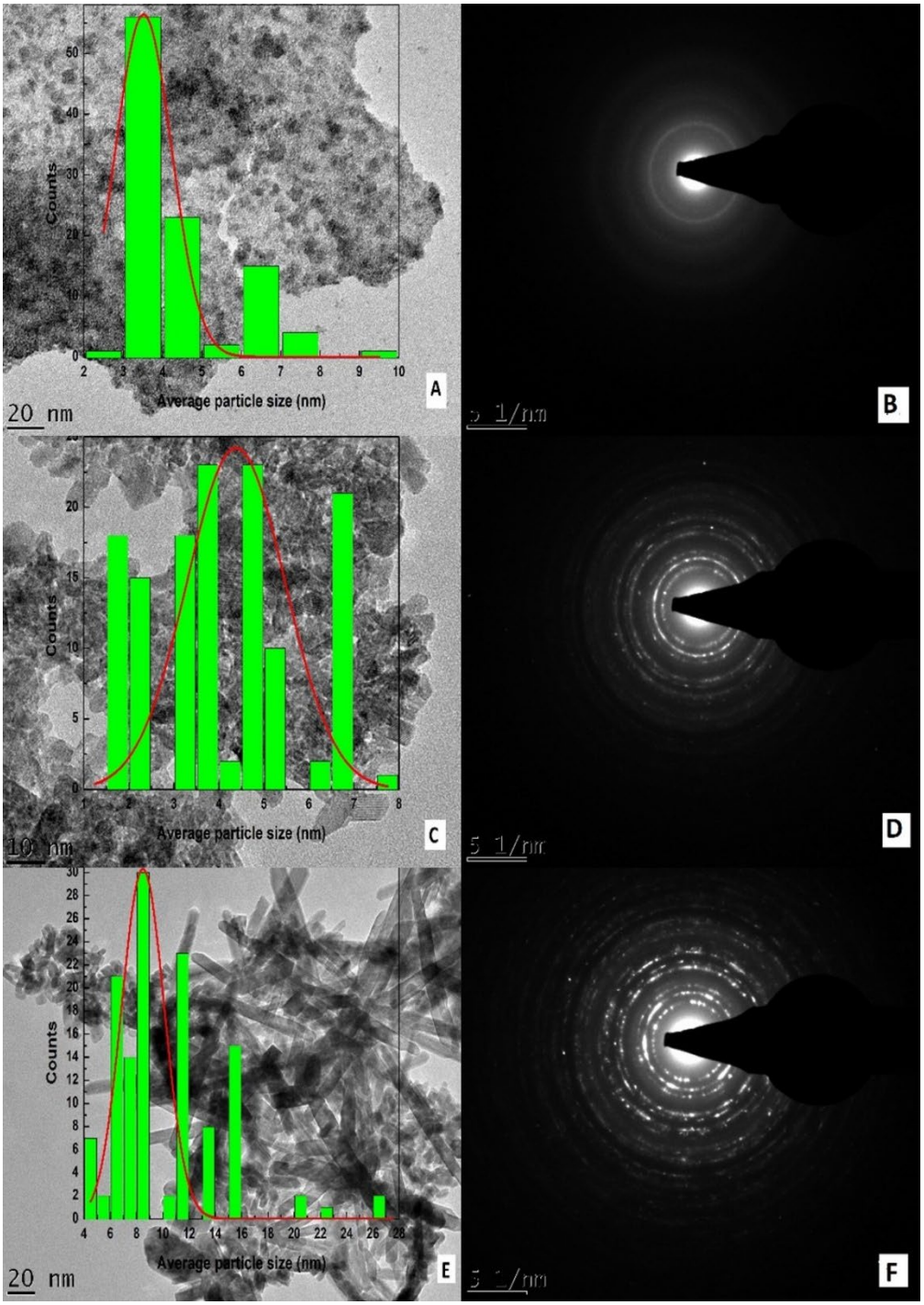

Figure 4.18: HRTEM and SAED analysis of (A) and (B) MSM-350-4-NaCl, (C) and (D) MSM-500-4-NaCl, and (E) and (F) MSM-650-4-NaCl.

Table 4.20: Average HRTEM particle sizes of commercial IrO_2 and IrO_2 synthesized using the MSM at temperatures 350, 500, and 650℃.

Sample name	Average particle size (nm)
MSM-350-4-NaCl	4.12
MSM-500-4-NaCl	4.74
MSM-650-4-NaCl	Width: 2.73 Length: 26.36
Commercial IrO_2	8.69

The N_2 adsorption-desorption analysis of the commercial IrO_2 and IrO_2 synthesized with the MSM are summarized in Table 4.21. The BET surface area of the synthesized IrO_2 increased with decrease synthesis temperatures. MSM-350-4-NaCl has the largest BET surface area of about 63.89 m^2/g. At increased temperatures i.e., 650℃, MSM-650-4-NaCl has a smaller BET surface area which is an indication of the larger IrO_2 particles, as revealed by the HRTEM analysis.

Table 4.21: BET surface areas of the commercial IrO_2 and IrO_2 synthesized using the MSM at temperatures 350, 500, and 650℃.

Sample name	BET surface area (m^2/g)
MSM-350-4-NaCl	63.89
MSM-500-4-NaCl	55.62
MSM-650-4-NaCl	31.77
Commercial IrO_2	25.11

The cyclic voltammograms were obtained at a potential scan rate of 20 mVs^{-1} between a potential of 0 and +1.4 V vs. RHE. Table 4.22 summarizes the redox couples, Ir(III)/Ir(IV) and Ir(IV)/Ir(V). Figure 4.19 shows the Ir(III)/Ir(IV) and Ir(IV)/Ir(V) anodic oxidation peak for the MSM-350-4-NaCl, MSM-500-4-NaCl, and MSM-650-4-NaCl. The decreased voltammetric charge may be partly due to the particle growth reduction and partly due to the oxide dehydration with increased oxide bridge bonding [72]. An additional peak was seen at +0.59 V vs. RHE for MSM-350-4-NaCl, at both the forward (anodic) and reverse (cathodic) scans. The additional peak can also be seen

for the commercial IrO_2. However, an extra peak cannot be seen for MSM-500-4-NaCl and MSM-650-4-NaCl, which excludes the possibility of the peak being an oxidation/reduction sodium layer impurity. The additional peaks are almost certainly due to the presence of active Ir(III) sites on the IrO_2. A strong negative "tail", upon the cathodic potential scan at 0 V vs. RHE, was seen for MSM-500-4-NaCl and MSM-650-4-NaCl. This reflects their negative capacitive behaviour (H_{ads}) [68, 120]. Rasten et al. [72] confirm the influence the negative capacitive behaviour, depending on the surface area, had on the IrO_2 synthesized at increased temperatures.

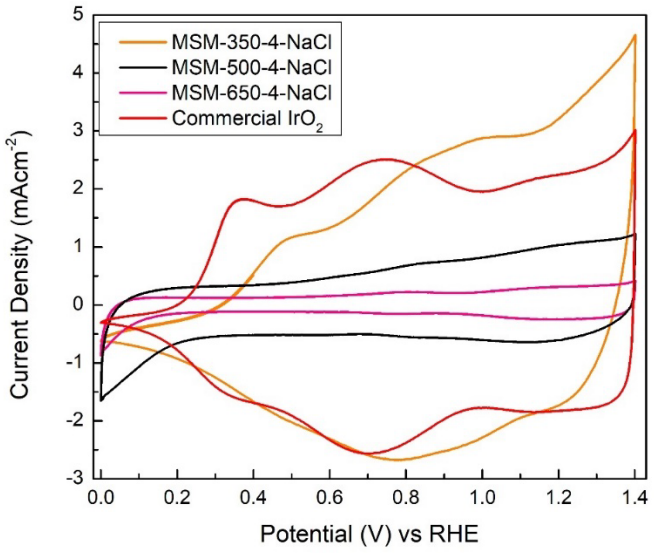

Figure 4.19: CV analysis in 0.5 M H_2SO_4 of the commercial IrO_2 and IrO_2 synthesized using the MSM temperatures 350, 500, and 650℃.

Table 4.22: Anodic peak potentials of the Ir(III)/Ir(IV) and Ir(IV)/Ir(V) redox couples of the commercial IrO_2 and IrO_2 synthesized using the MSM synthesized at 350, 500, and 650℃.

Sample name	Ir(III)/Ir(IV) redox couple (V vs. RHE)	Ir(IV)/Ir(V) redox couple (V vs. RHE)
MSM-350-4-NaCl	+0.97	+1.20
MSM-500-4-NaCl	+0.80	+1.23
MSM-650-4-NaCl	+0.78	+1.17
Commercial IrO_2	+0.74	+1.16

Figure 4.20 shows the polarization curves obtained using the LSV technique, between +1.0 and +1.8 V vs. RHE at a potential scan rate of 2 mVs^{-1}. Table 4.23 summarizes the OER overpotential, electrode potential at different current densities, and the Tafel slopes of the IrO_2. The MSM-350-4-NaCl had the lowest overpotential, at 10 $mAcm^{-2}$, when compared to MSM-500-4-NaCl and MSM-650-4-NaCl. At lower current densities (50 $mAcm^{-2}$), the MSM-350-4-NaCl had a higher OER activity. The lower OER activities of MSM-650-4-NaCl can be attributed to the larger particle sizes, along with the presence of metallic Ir shown by the HRTEM analysis. However, at increased current densities (150 $mAcm^{-2}$), the MSM-500-4-NaCl had higher OER activities. When comparing the Tafel slopes, MAFM-500-4-NaCl had the smallest Tafel slope.

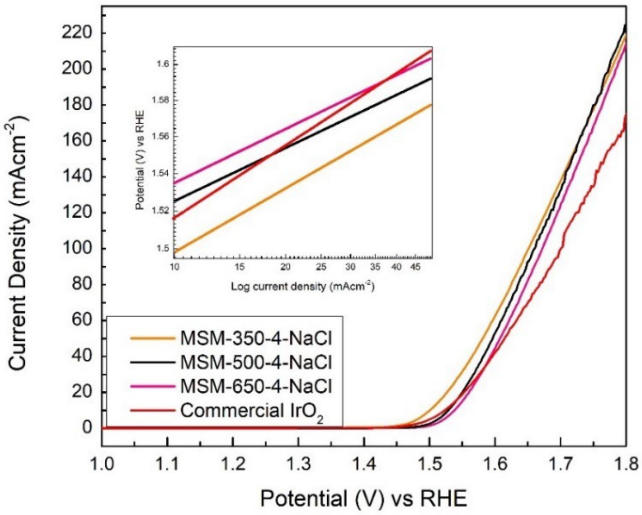

Figure 4.20: LSV analysis in 0.5 M H_2SO_4 of the commercial IrO_2 and IrO_2 synthesized with the MSM at temperatures 350, 500, and 650℃.

Table 4.23: Overpotential, electrode potentials, and the Tafel slopes of the commercial IrO_2 and IrO_2 synthesized with the MSM at temperatures 350, 500, and 650℃.

Sample name	Overpotential at 10 $mAcm^{-2}$ (V vs. RHE)	Onset potential at 50 $mAcm^{-2}$ (V vs. RHE)	Onset potential at 150 $mAcm^{-2}$ (V vs. RHE)	Tafel slopes 10-50 $mAcm^{-2}$ ($mV\ dec^{-1}$)
MSM-350-4-NaCl	0.27	1.58	1.71	40.54
MSM-500-4-NaCl	0.30	1.59	1.73	40.45
MSM-650-4-NaCl	0.31	1.61	1.73	40.46
Commercial IrO_2	0.29	1.62	1.77	40.32

The CP analysis was performed at 10 $mAcm^{-2}$ until the potential reached a cut-off of 1.8 V vs. RHE. Figure 4.21 shows the OER stability of the IrO_2 synthesized using the MSM at temperatures 350, 500, and 650℃. MSM-500-4-NaCl had the highest stability of ~75 hrs. The performance of MSM-650-4-NaCl was initially affected by bubble formation on the WE. The commercial IrO_2 was the least stable when compared to the synthesized IrO_2 due to IrO_2 dissolution which are caused by degradation [118]. Table 4.24 summarizes the OER stability of the commercial IrO_2 and IrO_2 synthesized with

the MSM. Lim et al. [79] reported similar behaviour with higher crystallinity exhibiting a higher OER stability.

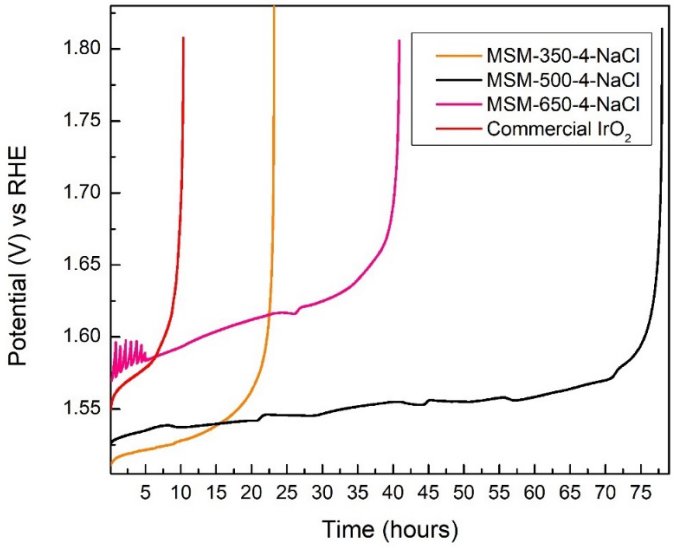

Figure 4.21: CP analysis in 0.5 M H_2SO_4 of the commercial IrO_2 and IrO_2 synthesized using the MSM at temperatures 350, 500, and 650℃.

Table 4.24: OER stability of the commercial IrO_2 and IrO_2 synthesized using the MSM at temperatures 350, 500, and 650℃.

Sample name	Stability (hrs)
MSM-350-4-NaCl	23.2
MSM-500-4-NaCl	75.2
MSM-650-4-NaCl	40.9
Commercial IrO_2	10.4

4.3 Summary of the best performing IrO_2 catalyst

A commercial IrO_2 was used as a benchmark to compare the OER performances of the IrO_2 synthesized with the MAFM and MSM, as shown in Table 4.25. For the MAFM, sample MAFM-350-2-$NaNO_3$ showed the highest OER activity at current densities <150 $mAcm^{-2}$. At higher current densities, MAFM-500-2-$NaNO_3$ showed improved OER activities and has the smallest Tafel slope (40.24 $mVdec^{-1}$). MAFM-350-2-$NaNO_3$

showed the highest OER stability, with the commercial IrO_2 only out-performing the stability of MAFM-650-2-$NaNO_3$. For the MSM, sample MSM-350-4-NaCl also showed higher OER activities at current densities <150 $mAcm^{-2}$. MSM-500-4-NaCl showed higher OER activities at increased current densities. All the IrO_2 synthesized with the MSM showed improved OER stabilities when compared to the commercial IrO_2, with MSM-500-4-NaCl showing the highest stability. When comparing the IrO_2 from both the MAFM and MSM, the lowered synthesis temperature, i.e., 350℃, produced improved OER performances.

Figure 4.25: Summary of the OER performances of the commercial IrO_2 and IrO_2 synthesized with the MAFM and MSM.

Sample name	**Crystallite size (nm)**	**Morphology (nm)**	**BET surface area (m^2/g)**	**Ir(III)Ir(IV)/ Ir(IV)Ir(V) redox couples (V vs. RHE)**	**Overpotential (V vs. RHE)**	**Stability (hrs)**
MAFM-350-2-$NaNO_3$	2.73	2.31	216.23	+0.94/+1.30	0.28	81.80
MAFM-350-2-KNO_3	2.41	2.08	167.52	+0.74/+1.26	0.31	20.82
MAFM-500-2-$NaNO_3$	7.78	3.54	104.84	+0.82/+1.28	0.29	44.30
MAFM-650-2-$NaNO_3$	10.01	Width: 5.23 Length: 11.36	53.84	+0.78/+1.18	0.36	5.50
MSM-350-4-NaCl	2.83	4.12	63.89	+0.97/+1.20	0.27	23.2
MSM-500-4-NaCl	7.05	4.74	55.62	+0.80/+1.23	0.30	75.2
MSM-650-4-NaCl	12.43	With: 2.73 Length: 26.36	31.77	+0.78/+1.17	0.31	40.9
MSM-650-8-NaCl	8.78	8.18	54.69	+0.79/+1.19	0.32	22.4
Commercial IrO_2	0	8.69	25.11	+0.74/+1.16	0.29	10.40

Chapter 5: Conclusion and recommendations

5.1 Conclusion

In the PEMWE, IrO_2 is the most stable catalyst for the OER, however, its activity needs further improvement [20, 35]. This study set out to synthesize an IrO_2 catalyst with both improved activity and stability for the OER by tailoring both physical and electronic properties by optimizing the synthesis method. Different methods can be used to synthesize IrO_2. In this study, the MAFM and MSM were chosen to synthesize the IrO_2 catalyst due to their high stability, simplicity, eco-friendly, and cost-effectiveness. The IrO_2 catalysts were compared to a benchmark commercial IrO_2. Both the physical (XRD, HRTEM, and BET) and electrochemical characterizations (CV, LSV, and CP) were used to evaluate the validity of the synthesized IrO_2 as an OER catalyst in PEMWE.

The optimization of the synthesis conditions proved essential to synthesize IrO_2 with improved OER performances. For the MAFM, MAFM-350-2-$NaNO_3$ exhibited the best OER activity and stability, when compared to a commercial IrO_2. The HRTEM analysis revealed IrO_2 particles of up to 3 nm, which increased the BET active surface area. This further proved that MAFM-350-2-$NaNO_3$ is a highly efficient anode catalyst for the PEMWE. Furthermore, improved OER performances can also be seen by MAFM-350-2-KNO_3. MAFM-650-2-$NaNO_3$ showed the lowest OER activity and stability. The XRD analysis revealed the IrO_2 crystallinity increased with increase synthesis temperature. The sample's larger particle sizes decreased the BET active surface area which may explain the lower OER performances. For the MSM, MSM-350-4-NaCl also showed significant improvement in the OER activity when compared to the commercial IrO_2. MSM-500-4-NaCl exhibit the best OER stability. When optimizing the synthesis duration, MSM-650-4-NaCl showed improved OER performances than both MSM-650-8-NaCl and the commercial IrO_2. By increasing the synthesis duration, both the sample's crystallinity and particle sizes increased, as shown by XRD and HRTEM analyses, which decreased its active BET surface area.

Both the MAFM and MSM synthesized IrO_2 with improved OER performances when compared to the commercial IrO_2. This shows the IrO_2 catalyst can be enhanced significantly by simply adjusting the synthesis conditions and method, thus improving the IrO_2 catalyst's physical properties. Such improved OER performances may result in lower catalytic loading requirements, which lowers the cost related to the PEMWE.

5.2 Recommendations

From the obtained outcome, recommendations concerning future investigations are listed below:

- Further analysis, for the MSM, of either solvent KCl or a combination between KCl and NaCl is required to explain the OER performance mechanism of MSM-350-4-NaCl.

- The change scan rates in the CV analysis, on IrO_2 synthesized with the MSM, requires further investigation.

- Further characterization techniques, including SEM, XPD, and SCSA, are necessary to study the chemical and structural properties of the IrO_2 catalysts, especially those produced at lower synthesis temperatures.

- The IrO_2 catalyst with the highest OER performance needs to be examined in a PEMWE single cell.

References

[1] Lubitz W, Tumas W. Hydrogen: An Overview. Journal of Chemical Reviews. 2007;107(10):3900-3903.

[2] Balat M. Possible Methods for Hydrogen Production. Journal of Energy Sources. 2008;31(1):39-50.

[3] Conte M, Iacobazzi A, Ronchetti M, and Vellone R. Hydrogen economy for a sustainable development: state-of-the-art and technological perspectives. Journal of Power Sources. 2001;100(2):171-187.

[4] Mazloomi K, Gomes C. Hydrogen as an energy carrier: Prospects and challenges. Renewable and Sustainable Energy Reviews. 2012;16(5):3024-3033.

[5] Momirlan M, and Veziroglu T. Current status of hydrogen energy. Renewable and Sustainable Energy Reviews. 2002;6(2):141-179.

[6] Olladay J, Hu J, King D, Wang Y. An overview of hydrogen production technologies. Journal of Catalysis Today. 2009:139;244-260.

[7] Nikolaidis P, Poullikkas A. A comparative overview of hydrogen production processes. Journal of Renewable and Sustainable Energy Reviews. 2017:67;597-611.

[8] Laguna-Bercero M. Recent advances in high temperature electrolysis using solid oxide fuel cells: A review. Journal of Power Sources. 2012;203:4-16.

[9] Turner J, Sverdrup G, Mann M, Maness P, Kroposki B, Ghirardi M, Evans R, Blake D. Renewable hydrogen production. International Journal of Energy Research. 2008;32:379-407.

[10] Pregger T, Graf D, Krewitta W, Sattler, Roeb M, Mo S. Prospects of solar thermal hydrogen production processes. International Journal of Hydrogen Energy. 2009;34:4256–4267.

[11] Puthiyapura V., Development of anode catalysts for Proton Exchange Membrane Water Electrolyser [dissertation]. Newcastle: Newcastle University; 2014.

[12] Barbir F. PEM electrolysis for production of hydrogen from renewable energy sources. Journal of Solar Energy. 2005;78:661–669.

[13] Dawood F, Anda M, Shafiullah G. Hydrogen production for energy: An overview. International Journal of Hydrogen Energy. 2020;45:3847-3869.

[14] Gu X, Yuan S, Ma M, Zhu J. Nanoenhanced Materials for Photolytic Hydrogen Production [dissertation]. Sweden: Department of Chemistry; 2017.

[15] Best J, Dunstan D. Nanotechnology for photolytic hydrogen production: Colloidal anodic oxidation. International Journal of Hydrogen Energy.2009;34:7562-7578.

[16] Dincer I. Green methods for hydrogen production. International Journal of Hydrogen Energy.2012;37:1954-1971.

[17] Holladay J, Hu J, King D, Wang Y. An overview of hydrogen production technologies. Journal of Catalysis Today. 2009;139(4):244-260.

[18] Bičáková O, Straka P. Production of hydrogen from renewable resources and its effectiveness. International Journal of Hydrogen Energy. 2012;37(16):11563-11578.

[19] Balat M. Potential importance of hydrogen as a future solution to environmental and transportation problems. International Journal of Hydrogen Energy. 2008;33(15):4013-4029.

[20] Kumar S, Himabindu V. Journal of Materials Science for Energy Technologies. 2019;2:442–454.

[21] Turner J. Sustainable Hydrogen Production, Journal of Science. 2004;305(5686):972-974.

[22] Marshall A. Electrocatalysts for the oxygen evolution electrode in water electrolysers using proton exchange membranes: synthesis and characterization

[dissertation]. Norwegian: Norwegian University of Science and Technology; 2005.

[23] Neagu C, Jansen H, Gardeniers H, Elwenspoek M. The electrolysis of water: an actuation principle for MEMS with a big opportunity. Journal of Mechatronics. 2000;10:571-581.

[24] Ni M, Leung M, Leung D. Energy and exergy analysis of hydrogen production by a proton exchange membrane (PEM) electrolyzer plant. Journal of Energy Conversion and Management. 2008;49:2748–2756.

[25] Zhang J. PEM Fuel Cell Electrocatalysts and Catalyst Layers Fundamentals and Applications. Canada: Springer; 2008.

[26] Pletcher D, Li X. Prospects for alkaline zero gap water electrolysers for hydrogen production. International Journal of Hydrogen Energy. 2011;36(23):15089-15104.

[27] Ursu A, Gandı L, Sanchis P. Hydrogen Production From Water Electrolysis: Current Status and Future Trends. Journal of Hydrogen Enegry. 2012;100(2).

[28] Skulimowska A, Dupont M, Zaton M, Sunde S, Merlo L, Jones D, Rozie J. Proton exchange membrane water electrolysis with short-side-chain Aquivion membrane and IrO_2 anode catalyst. International Journal of Hydrogen Energy. 2014;39:6307-6316.

[29] Marini S, Salv P, Nelli P, Pesenti R, Villa M, Berrettoni M, Zangari G, Kiros Y. Advanced alkaline water electrolysis. Journal of Electrochimica Acta. 2012;82:384-391.

[30] Carmo M, Fritz D, Mergel J, Stolten D. A comprehensive review on PEM water electrolysis. International Journal of Hydrogen Energy. 2013;38:4901-4934.

[31] Chi J, Yu H. Water electrolysis based on renewable energy for hydrogen production. Chinese Journal of Catalysis. 2018;39:390–394.

[32] Haug P, Kreitz B, Koj M, Turek T. Process modelling of an alkaline water electrolyzer. International Journal of Hydrogen Energy. 2017;42:15689-15707.

[33] Gandı L, Oroz R, Ursu A, Sanchis P, Die´guez P. Renewable Hydrogen Production: Performance of an Alkaline Water Electrolyzer Working under Emulated Wind Conditions. Journal of Energy and Fuels. 2007;21:1699-1706.

[34] Stempiena J, Sun Q, Chan S. Solid Oxide Electrolyzer Cell Modeling: A Review. Journal of Power Technologies. 2013;93(4):216–246.

[35] Arico A, Siracusano S, Briguglio N, Baglio V, Blasi A, Antonucci V. Polymer electrolyte membrane water electrolysis: status of technologies and potential applications in combination with renewable power sources. Journal of Applied Electrochemistry. 2013;43:107–118.

[36] Nguyena M, Ranjbari A, Catala L, Brisset F, Brisset P, Aukauloo A. Implementing molecular catalysts for hydrogen production in proton exchange membrane water electrolysers. Journal of Coordination Chemistry Reviews. 2012;256:2435–2444.

[37] Wendt H, Imarisio G. Nine years of research and development on advanced water electrolysis: A review of the research programme of the Commission of the European Communities. Journal of Applied Electrochemistry. 1988;18(1):1-14.

[38] Zayat B, Mitra D, Narayanan S. Inexpensive and Efficient Alkaline Water Electrolyzer with Robust Steel-Based Electrodes. Journal of The Electrochemical Society. 2020;167(114513).

[39] Doenitz W, Schmidberger R, Steinheil E, Screicher R. Hydrogen production by high temperature electrolysis of water vapour. International Journal of Hydrogen Energy. 1980;5:55-63.

[40] Ni M, Leung M, Leung D. Technological development of hydrogen production by solid oxide electrolyzer cell (SOEC). International Journal of Hydrogen Energy. 2008;33:2337-2354.

[41] Ghadgea S, Patel P, Dattab M, Velikokhatnyib O, Shanthia P, Kumta P. First report of vertically aligned (Sn,Ir)O2:F solid solution nanotubes: Highly efficient and robust oxygen evolution electrocatalysts for proton exchange

membrane based water electrolysis. Journal of Power Sources. 2018;392:139-149.

[42] Millet P. Hydrogen Energy, Germany: Publisher Wiley-VCH Verlag GmbH & Co. KGaA; 2015.

[43] Selamet O, Becerikli F, Mat M, Kaplan Y. Development and testing of a highly efficient proton exchange membrane (PEM) electrolyzer stack. International Journal of Hydrogen Energy. 2011;36:11480-11487.

[44] Falcao D, Pinto A. A review on PEM electrolyzer modelling: Guidelines for beginners. Journal of Cleaner Production. 2020;261(121184).

[45] Nakamura T. Hydrogen production from water utilizing solar heat at high temperatures. Journal of Solar Energy. 1977;19:467—475.

[46] Rozain C, Millet P. Electrochemical characterization of Polymer Electrolyte Membrane Water Electrolysis Cells. Journal of Electrochimica Acta. 2014;131:160–167.

[47] Ayers K. The potential of proton exchange membrane–based electrolysis technology. Journal of Current Opinion in Electrochemistry. 2019;18:9-15.

[48] Grigoriev S, Pushkarev A, Pushkareva I, Millet P, Belov A, Novikov V, Belaya I, Voloshin Y. Hydrogen production by proton exchange membrane water electrolysis using cobalt and iron hexachloroclathrochelates as efficient hydrogen-evolving electrocatalysts. International Journal of Hydrogen Energy. 2017;42:27845-27850.

[49] Appel A, Helm M. Determining the Overpotential for a Molecular Electrocatalyst. Journal of Catalysis. 2014;4:630−633.

[50] Maric R, Yu H. Proton Exchange Membrane Water Electrolysis as a Promising Technology for Hydrogen Production and Energy Storage. United States of America: Publisher InterchOpen; 2018.

[51] Van de Merwe J, Uren K, Van Schoor G, Bessarabov D. Characterisation tools development for PEM electrolysers. International Journal of Hydrogen Energy. 2014;39:14212-14221.

[52] Lide D. CRC Handbook of Chemistry and Physics. National Institute of Standards and Technology; 2003.

[53] Cheng J, Zhang H, Ma H, Zhong H, Zou Y. Study of carbon-supported IrO_2 and RuO_2 for use in the hydrogen evolution reaction in a solid polymer electrolyte electrolyzer. Journal of Electrochimica Acta. 2010;55(5):1855-1861.

[54] Sheng W, Gasteiger H, Shao-Horn Y. Hydrogen Oxidation and Evolution Reaction Kinetics on Platinum: Acid vs Alkaline Electrolytes. Journal of The Electrochemical Society. 2010;157(11):B1529-B1536.

[55] Conway B, Jerkiewicz G. Relation of energies and coverages of underpotential and overpotential deposited H at Pt and other metals to the 'volcano curve' for cathodic H_2 evolution kinetics. Journal of Electrochimica Acta. 2000;45(25):4075-4083.

[56] Grrele y J, Jaramillo T, Bonde J, Chorkendoriff I, Norskou J. Computational high-throughput screening of electrocatalytic materials for hydrogen evolution. Journal of Nature Materials. 2006;5(11):909-913.

[57] Trasatti S. Work function, electronegativity, and electrochemical behaviour of metals: III. Electrolytic hydrogen evolution in acid solutions. Journal of Electroanalytical Chemistry and Interfacial Electrochemistry. 1972;39(1):163-184.

[58] Laursen A, Varela A, Dionigi F, Fanchiu H, CMiller C, Trinhammer O, Rossmeisl J, Dahl S. Electrochemical Hydrogen Evolution: Sabatier's Principle and the Volcano Plot. Journal of Chemical Education. 2012;89(12):1595-1599.

[59] Rasten E. Electrocatalysis in Water Electrolysis with Solid Polymer Electrolyte [dissertation]. Norwegian: Norwegian University of Science and Technology; 2001.

[60] Damjanovic A, Dey A, Bockris J. Kinetics of oxygen evolution and dissolution on platinum electrodes. Journal of Electrochimica Acta. 1966;11(7):791-814.

[61] Trasatti S, Lodi G. Electrodes of conductive metallic oxides, Part B1980: Elsevier scientific publishing company.

[62] Beer H. The Invention and Industrial Development of Metal Anodes. Journal of The Electrochemical Society. 1980;127(8):303C-307C.

[63] Rasiyah P, Tseung A. The Role of the Lower Metal Oxide/Higher Metal Oxide Couple in Oxygen Evolution Reactions. Journal of The Electrochemical Society. 1984;131(4):803-808.

[64] Lee B, Ahna S, Parka H, Choi I, Yoo S, Kima H, Henkensmeier D, Kima J, Park S, Nama S, Lee K, Jang J. Development of electrodeposited IrO_2 electrodes as anodes in polymer electrolyte membrane water electrolysis. Journal of Applied Catalysis B: Environmental. 2015;179:285–291.

[65] Trasatti S. Electrocatalysis in the anodic evolution of oxygen and chlorine. Electrochimica Acta. 1984;29(11):1503-1512.

[66] Ahmed J, Mao Y. Ultrafine Iridium Oxide Nanorods Synthesized by Molten Salt Method toward Electrocatalytic Oxygen and Hydrogen Evolution Reactions. Journal of Electrochimica Acta. 2016;212:686–693.

[67] Tao L, Xu Y, Qian X, Yue Q, Kang Y. Low-Temperature Molten Salt Synthesis for Ligand-Free Transition Metal Oxide Nanoparticles. Journal of Applied Energy Material. 2020;3:3984−3990.

[68] Felix C, Bladergroen B, Linkov V, Pollet B, Pasupathi S. Ex-Situ Electrochemical Characterization of IrO_2 Synthesized by a Modified Adams Fusion Method for the Oxygen Evolution Reaction. Journal of Catalyst. 2019;9(318).

[69] Adams R, Shriner R. Platinum Oxide as a catalyst in the reduction of organic compounds.III Preparation and Properties of the oxide of Platinum obtained by the fusion of chloroplatinic acid with sodium nitrate. Journal of the American Chemical Society. 1923;45(9):2171-2179.

[70] Puthiyapura V, Pasupathi S, Basu S, Wu X, Su H, Aragunapandiyan N, Pollet B, Scott K. RuxNb1LxO_2 catalyst for the oxygen evolution reaction in proton exchange membrane water electrolysers. International Journal of Hydrogen Energy. 2013;38:8605-8616.

[71] Wu X, Tayal J, Basu S, Scott K. Nano-crystalline RuxSn1LxO2 powder catalysts for oxygen evolution reaction in proton exchange membrane water electrolysers. International Journal of Hydrogen Energy. 2011;36:14796-14804.

[72] Rasten E, Hagen G, Tunold R. Electrocatalysis in water electrolysis with solid polymer electrolyte. Journal of Electrochimica Acta. 2003;48:3945-3952.

[73] Zhang Y, Wang C, Mao Z, Wang N. Preparation of nanometer-sized SnO_2 by the fusion method. Journal of Materials Letters. 2007;61:1205-1209.

[74] Liu Y, Wang C, Lei Y, Liu F, Tian B, Wang J. Investigation of high-performance IrO_2 electrocatalysts prepared by Adams method. International journal of hydrogen energy. 2018;43:19460-19467.

[75] Cheng J, Zhang H, Ma H, Zhong H, Zou Y. Preparation of Ir0.4Ru0.6MoxOy for oxygen evolution by modified Adams' fusion method. International journal of hydrogen energy. 2009;34:6609-6613.

[76] Polonsky J, Petrushina I, Christensen E, Bouzek K, Prag C, Andersen J, Bjerrum N. Tantalum carbide as a novel support material for anode electrocatalysts in polymer electrolyte membrane water electrolysers. International journal of hydrogen energy. 2012;37:2173-2180.

[77] Zhou H, Mao Y, Wong S. Probing Structure-Parameter Correlations in the Molten Salt Synthesis of $BaZrO_3$ Perovskite Submicrometer-Sized Particles. Journal of Chemistry Materials. 2007;19:5238-5249.

[78] Mao Y. Facile Molten-salt synthesis of double perovskite La_2BMnO_6 nanoparticles. Journal of the Royal Society of Chemistry. 2012;2:12675-12678.

[79] Lim J, Park D, Jeon S, Roh C, Choi J, Yoon D, Park M, Jung H, Lee H. Ultrathin IrO_2 Nanoneedles for Electrochemical Water Oxidation. Journal of advanced functional materials. 2018;28:1704796.

[80] Bunaciu A, Udriştioiu E, Aboul-Enein H. X-Ray Diffraction: Instrumentation and Applications. Journal of a Critical Reviews in Analytical Chemistry. 2015;45:289–299.

[81] Chipera S, Bish D. Fitting Full X-Ray Diffraction Patterns for Quantitative Analysis: A Method for Readily Quantifying Crystalline and Disordered Phases. Journal of Advances in Materials Physics and Chemistry. 2013;3:47-53.

[82] Jenkins R, Snyder R. Introduction to X-Ray Powder Diffractometry. New York: John Wiley and Sons; 1996.

[83] Smart L, Moore E, Moore A, Smart L, Moore E. Solid state chemistry: an introduction. Boca Raton: Taylor & Francis; 2005.

[84] Cullity B. Elements of X-ray diffraction. United States: Addison-Wesley; 1956.

[85] Khan H, Yerramilli A, D'Oliveira A, Alford T, Boffito D, Patience G. Experimental methods in chemical engineering: X-ray diffraction spectroscopy-XRD. The Canadian journal of Chemical Engineering. 2020;98:1255-1266.

[86] Vander Wal R, Tomasek A, Pamphlet M, Taylor C, Thompson W. Analysis of HRTEM images for carbon nanostructure quantification. Journal of Nanoparticle Research. 2004;6:555–568.

[87] Gyoten H, Hirayama T, Kondo J, Taomoto A, Aizawa M. Quantitative TEM Analysis for the Pt Morphology in the Catalyst Layers of Polymer Electrolyte Membrane Fuel Cells. Journal of Electrochemistry. 2011;5:392-398.

[88] Yehliu K, Vander Wal R, Boehman A. Development of an HRTEM image analysis method to quantify carbon nanostructure. Journal of Combustion and Flame. 2011;158:1837–1851.

[89] Williams D, Carter B. Transmission Electron Microscopy A Textbook for Materials Science. United States of America: Publisher Springer Science; 2009.

[90] Reimschuessel A. Scanning electron microscopy - Part I. Journal of Chemical Education. 1972;49(8):413.

[91] Brunauer S, Emmett P, Teller E. Adsorption of Gases in Multimolecular Layers. Journal of the American Chemical Society. 1938;60(2):309-319.

[92] Tian Y, Wu J. A comprehensive analysis of the BET area for nanoporous materials. American Institute of chemical engineers journal. 2018;64(1).

[93] Mabbott G. An introduction to cyclic voltammetry. Journal of Chemical Education. 1983;60(9).

[94] Saddow S. Silicon carbide biotechnology: Biocompatible Semiconductor for Advanced Biomedical Devices and Applications. United States: Elsevier; 2016.

[95] Lowde D, Williams J, McNicol B. The Characterisation of catalyst surfaces by cyclic voltammetry. Journal of Applications of Surface Science. 1978;1:215—240.

[96] Macdonald D. Transient Techniques in Electrochemistry. United States: Plenum Press; 1977.

[97] Rountree E, McCarthy B, Eisenhart T, Dempsey J. Evaluation of Homogeneous Electrocatalysts by Cyclic Voltammetry. Journal of Inorganic Chemistry. 2014;53:9983−10002.

[98] Jürgen H. Cyclic Voltammetry-"Electrochemical Spectroscopy" New Analytical Methods. Angewandte Chemie International Edition in English. 1984;23(11):831-847.

[99] Riddiford A. Mechanisms for the evolution and ionization of oxygen at platinum electrodes. Journal of Electrochimica Acta. 1961;4(2):170-178.

[100] Marshall A, Børresen B, Hagen G, Sunde S, Tsypkin M, Tunold R. Iridium oxide-based nanocrystalline particles as oxygen evolution electrocatalysts. Russian Journal of Electrochemistry, 2042(10):1134-1140.

[101] Cheng J, Zhang H, Chen G, Zhang Y. Study of $Ir_xRu_{1-x}O_2$ oxides as anodic electrocatalysts for solid polymer electrolyte water electrolysis. Journal of Electrochimica Acta. 2009;54:6250–6256.

[102] Neol M, Chandrasekaran S, Basha C. Linear Sweep Voltammetry approach for the study of monolayer formation. Journal of Electroanalytical Chemistry. 1987;225:93-109.

[103] Gonzalez-Huerta R, Ramos-Sanchez G, Balbuena P. Oxygen evolution in Co-doped RuO_2 and IrO_2: Experimental and theoretical insights to diminish electrolysis overpotential. Journal of Power Sources. 2014;268:69-76.

[104] Escarpa A, Gonzalez M, Lopez M. Agricultural and food electrolysis. Mexico: Publisher John Wiley and Sons Ltd.; 2015.

[105] Bard A, Faulkner L. Electrochemical methods: Fundamentals and applications. United States: Publisher John Wiley and Sons Ltd.; 2001.

[106] Ma Z, Wang X. Reaction mechanism for oxygen evolution on RuO_2, IrO_2, and RuO_2@IrO_2 core-shell nanocatalysts. Journal of Electroanalytical Chemistry. 2017;819:296-305.

[107] Zoulias E, Varkaraki E, Lymberopoulos N, hristodoulou C, Karagiorgis G. A review on water electrolysis, Greece: Publisher Centre for Renewable Energy Sources (CRES); 2003.

[108] Qiu Z, Ma Y, Edstrom K, Niklasson G, Edvinsson T. Controlled crystal growth orientation and surface charge effects in self-assembled nickel oxide nanoflakes and their activity for the oxygen evolution reaction. International Journal of Hydrogen Energy. 2017;42:28397-28407.

[109] Paunovic M. Review: Chronopotentiometry. Journal of Electroanalytical Chemistry. 1967;14:447-474.

[110] Jain R, Gaur H. Chronopotentiometry: Review of theoretical principles. 1977;79:211-236.

[111] Lingane P, Peters D. Chronopotentiometry. Journal of Analytical Chemistry. 2008;1(4):587-634.

[112] Vukovic M, Pravdic V. Cyclic Chronopotentiometry: Determination of Types and Rates of Second Order Chemical Reactions Following Electron Transfer. Journal of Croatica Chemica Acta. 1970;43:31-32.

[113] Elgrishi N, Rountree K, McCarthy B, Rountree E, Eisenhart T, Dempsey J. A Practical Beginner's Guide to Cyclic Voltammetry. Journal of Chemical Education. 2018;95:197-206.

[114] Siracusano S, Baglio V, Blasi A, Briguglio N, Stassi A, Ornelas R, Trifoni E, Antonucci V, Arico A. Electrochemical characterization of single cell and short stack PEM electrolyzers based on a nanosized IrO_2 anode electrocatalyst. International Journal of Hydrogen Energy. 2010;35:5558-5568.

[115] Zuo X, Chen Z, Guan C, Chen K, Song S, Xiao G, Pang Y, Wang J. Molten Salt Synthesis of High-Performance: Nanostructured La0.6Sr0.4FeO3−δ Oxygen Electrode of a Reversible Solid Oxide Cell. Journal of Materials. 2020;13:2267.

[116] Marshall A, Børresen B, Hagen G, Tsypkin M, Tunold R. Electrochemical characterisation of $Ir_xSn_{1-x}O_2$ powders as oxygen evolution electrocatalysts. Journal of Electrochimica Acta. 2006;51:3161–3167.

[117] Steegstra P, Busch M, Panas I, Ahlberg E. Revisiting the Redox Properties of Hydrous Iridium Oxide Films in the Context of Oxygen Evolution. Journal of Physical Chemistry. 2013;117:20975–20981.

[118] Ouattara L, Fierro O, Koudelka M, Comninellis C. Electrochemical comparison of IrO_2 prepared by anodic oxidation of pure iridium and IrO_2 prepared by thermal decomposition of H_2IrCl_6 precursor solution. Journal of Applied Electrochemistry. 2009;39:1361-1367.

[119] Felix C, Maiyalagan T, Pasupathi S, Bladergroen B, Linkov V. Synthesis and optimisation of IrO_2 electrocatalysts by Adams fusion method for solid polymer electrolyte electrolysers. Journal of Micro and Nanosystems. 2012;4(3):186-191.

[120] Grupioni A, Arashiro E, Lassali T. Voltammetric characterization of an iridium oxide-based system: The pseudocapacitive nature of the Ir0.3Mn0.7O2 electrode. Journal of Electrochimica Acta. 2002;48:407-418.

[121] Lim J, Kang G, Lee J, Jeon S, Jeon H, Kang P. Amorphous Ir atomic clusters anchored on crystalline IrO_2 nanoneedles for proton exchange membrane water oxidation. Journal of Power Sources. 2022;524:231069.

[122] Han S, Mo Y, Lee Y, Lee S, Park D, Park K. Mesoporous iridium oxide/Sb-doped SnO_2 nanostructured electrodes for polymer electrolyte membrane water electrolysis. International Journal of Hydrogen Energy. 2020;45(3):1409-1416.

[123] Subramaniana V, Hall S, Smith P, Rambabu B. Mesoporous anhydrous RuO_2 as a supercapacitor electrode material. Journal of Solide State Ionics. 2004;175:511-515.

[124] Feng Q, Yuan X, Liu G, Wei B, Zhang Z, Li H, Wang H. A review of proton exchange membrane water electrolysis on degradation mechanisms and mitigation strategies. Journal of Power Sources. 2017;366:33-55.